ISPRS Journal of Photogrammetry and Remote Sensing 191 (2022) 68–84

Contents lists available at ScienceDirect

ISPRS Journal of Photogrammetry and Remote Sensing

journal homepage: www.elsevier.com/locate/isprsjprs

Spatio-temporal characterization of surface water dynamics with Landsat in endorheic Cuvelai-Etosha Basin (1990–2021)

Eliakim Hamunyela [a,*], Martin Hipondoka [a], Frans Persendt [a], Hilma Sevelia Nghiyalwa [a], Chris Thomas [a,b], Kenneth Matengu [c]

[a] Department of Environmental Science, Faculty of Agriculture, Engineering and Natural Sciences, University of Namibia, Private Bag 13301, Windhoek, Namibia
[b] Lincoln Centre for Water & Planetary Health, College of Science, University of Lincoln. Brayford Pool, Lincoln, Lincolnshire LN6 7TS, United Kingdom
[c] Office of the Vice Chancellor, University of Namibia, Private Bag 13301, Windhoek, Namibia

ARTICLE INFO

Keywords:
Surface water
Landsat
Cuvelai-Etosha
Endorheic basin
Flooding
Angola
Namibia

ABSTRACT

Socio-economic damages caused by extreme floods have been increasing rapidly in recent years, mainly driven by changes in the climate and modulated by increasing human population in deltic areas and floodplains. The Cuvelai-Etosha Basin (CEB) in southern Africa, covering southern Angola and northern Namibia, experiences socially and economically devastating extreme floods. Yet, accurate information on past and current surface water changes and dynamics is lacking. Here, we estimate and map the surface water extents in the CEB and its surroundings (CEB + S) for 32 years (1990–2021) from Landsat data using random forest models to provide long-term baseline information on surface water changes and dynamics. Based on the reference data, a total of 15,677 ± 1080 km^2 have been inundated by surface water in the CEB + S during 1990–2021. This extent was accurately mapped by our local water extent product (mapped area = 16,273 km^2, user's accuracy = 91.5 ± 2.5%, producer's accuracy = 91.1 ± 6%). With user's and producer's accuracy of 91%, our overall water extent provides the first most accurate long-term baseline information on surface water inundation in CEB + S necessary for local spatial planning processes to minimise future negative impacts of floods in the basin. Interannual variability of surface water extent is, however, high, with water extent ranging from 520.8 ± 375.7 km^2 to 12372.3 ± 1154.7 km^2 during the 1990–2021 period. The largest annual water extents (>10,000 km^2) were recorded in 2006, 2008, 2009, 2011, and 2017, whereas the smallest extents (<1000 km^2) were recorded in 1992 and 2019. We found that over 40% of the area inundated in the CEB + S during 1990–2021 was inundated less than 9 times. With human population increasing rapidly in the CEB + S, rarely inundated areas with short water residence could become a prime target for human settlements, which may lead to huge socio-economic damages during extreme floods if no preventive measures are put in place. Globally available surface water maps from the Global Land Analysis and Discovery (GLAD) and European Commission's Joint Research Centre (JRC) did not provide realistic surface water extent for CEB + S, especially during years with extreme floods. Therefore, locally adopted product for operational monitoring of surface water in the CEB + S is needed to provide accurate information for informing spatial planning processes and surface water resource management strategies in this endorheic basin and help minimise future negative impacts of floods.

1. Introduction

Deltic systems and floodplains offer unique opportunities for socio-economic growth (Mazzoleni et al., 2021) but socio-economic costs of extreme floods are drastically increasing in many of these systems (Allaire, 2018; Álvarez, et al., 2019; Svetlana et al., 2015) because people are increasingly settling in flood-prone areas (Di Baldassarre et al., 2010; Mazzoleni et al., 2021; Tellman et al., 2021) probably due to rapid population growth in many parts of the world (Gerland et al., 2014; United Nations, 2017). With climatic and weather extremes increasing and becoming more intense (Easterling et al., 2000; Milly et al., 2002; Rahmstorf and Coumou, 2011; Kundzewicz et al., 2014; Pohl et al., 2017; Kendon et al., 2019), socio-economic costs of extreme floods are likely to further increase in deltic systems across the globe. A

* Corresponding author.
E-mail address: hamunyelae@unam.na (E. Hamunyela).

https://doi.org/10.1016/j.isprsjprs.2022.07.007
Received 3 December 2021; Received in revised form 4 July 2022; Accepted 8 July 2022
Available online 15 July 2022

key step in minimising the impacts of extreme floods in these systems is to integrate accurate spatio-temporal information on surface water change and dynamic into local spatial planning processes. However, such information is lacking for many human-inhabited water basins. Of particular concern are the basins with highly dynamic hydrology but predominantly ungauged, which are widespread in semi-arid, data-scarce areas in Africa.

Satellite remote sensing offers capacity to continuously monitor and produce surface water maps at various spatio-temporal scales (Alsdorf et al., 2007; Halabisky et al., 2016; Li et al., 2018; Pekel et al., 2016; Seiler et al., 2009; Tulbure et al. 2016) which can fill the gaps in poorly ungauged basins. The benefits of integrating spatio-temporal information in local planning processes are well recognised. In Australia, for example, the 2011 extreme floods caused severe socio-economic damages and triggered the government to initiate a country-wide multi-year mapping of surface water using earth observation data and obtain accurate spatio-temporal information on surface water change and dynamics to support local planning (Mueller et al., 2016). With the opening of Landsat archives in 2008 (Wulder et al., 2012), temporally consistent and free-to-use satellite imagery spanning over 40 years are now available, and has since been instrumental in improving our understanding of global surface water dynamics (Feng et al., 2016; Pekel et al., 2016; Pickens et al., 2020) and in many local settings (Deng et al., 2019; Mueller et al., 2016; Tulbure et al., 2016; Tulbure et al., 2014; Xia et al., 2019). The 10 m resolution imagery from Copernicus Sentinel-2A and-2B satellites provide even more spatially enhanced capability than Landsat to map surface water (Yang et al., 2020) but data from these satellites are only available since 2015, and do not yet provide elaborate historical information on changes and dynamics of surface water. In addition to providing historical baseline information, satellite data can also be used for near real-time mapping and monitoring of surface water (DeVries et al., 2020; Pekel et al., 2014). However, capturing short-lived flash floods remain challenging due to the long revisit frequency of satellites with appropriate spatial resolution for mapping floods at local scale. Cloud cover is also a key obstacle to accurate mapping of flash floods, but recent availability of multi-temporal optical satellite data and free Synthetic Aperture Radar (SAR) data has enhanced the capability to map surface water despite cloud cover (DeVries et al., 2020; Hardy et al., 2019; De Groeve, 2010). Despite recent methodological advancements in surface water mapping (Feyisa et al., 2014; Isikdogan et al., 2017; Tulbure et al., 2016; Isikdogan et al., 2017; Lary et al., 2016) coupled with the availability of free-to use satellite data covering several decades (Loveland and Dwyer, 2012; Loveland and Irons 2016; Wulder et al., 2012, 2015), accurate spatio-temporal information on surface water changes and dynamics is still lacking for many human-inhabited basins which experience extreme floods. In such basins, publicly available global surface water datasets (e.g. Pekel et al., 2016; Pickens et al., 2020) generated from Landsat data have become an alternative data-source for local spatial planning and surface water monitoring activities. Yet, the local utility of global surface water datasets to support effective spatial planning and surface water monitoring remains unknown in many basins. However, a recent study highlighted the need for regional and local maps of land-cover datasets in times of global change as global datasets often fail to capture local changes which are relevant for planning at local and regional level (Tulbure et al., 2022b).

The Cuvelai-Etosha Basin (CEB) in southern Africa, covering southern Angola and northern Namibia, does not have accurate spatio-

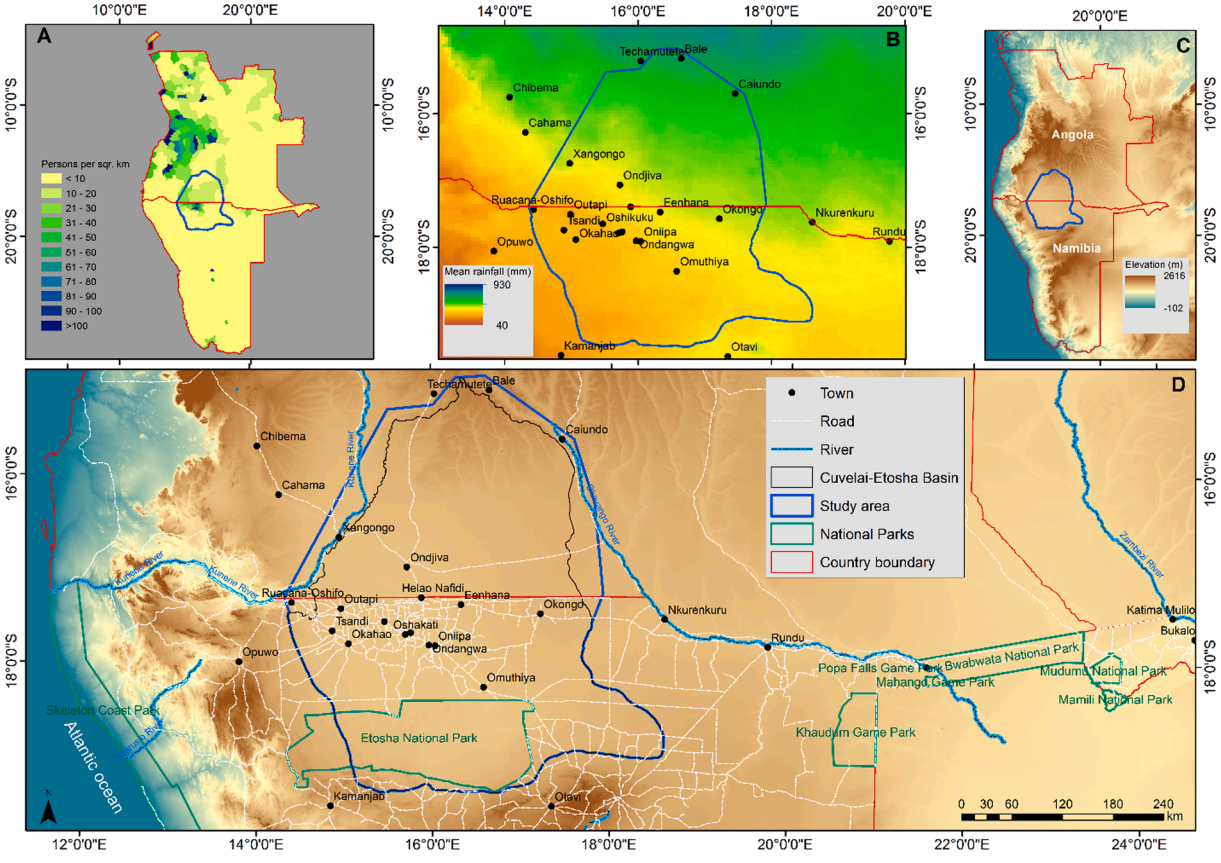

Fig. 1. The location of the study area and the Cuvelai-Etosha Basin. Population density (A) was calculated using population data from 2011 Population and Housing Census for the Namibian side, and 2014 Population and Housing Census for the Angolan side. Temporal mean rainfall (B) is based on the CHIRPS gridded rainfall estimates (Funk et al., 2014) for 1990–2021 period. The elevation (C) is based on the Advanced Land Observing Satellite (ALOS) Digital Surface Model (AW3D30). A zoom-in (D) of the study area showing towns, road, perennial rivers and protected wildlife areas.

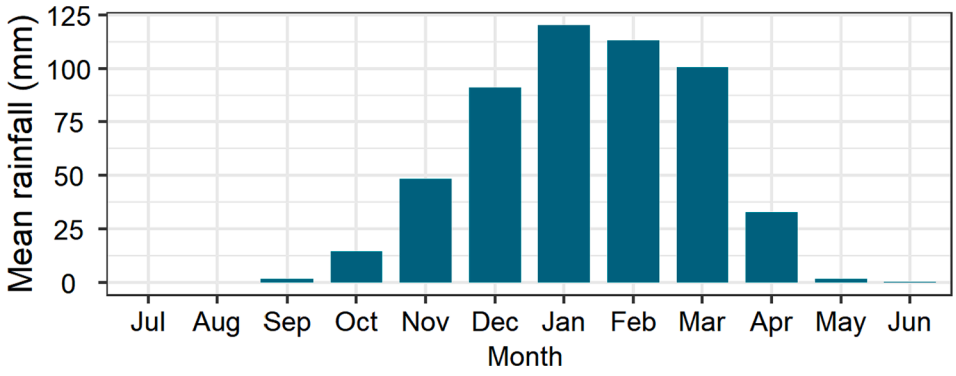

Fig. 2. Monthly mean rainfall for the study area during the 1990–2021 period based on the CHIRPS gridded rainfall estimates (Funk et al., 2014). The rainfall for each month per year was first averaged spatially before calculating the temporal monthly mean.

temporal information on surface water changes and dynamics. Yet, this seasonally inundated endorheic water basin is inhabited by more than 1.3 million people (Namibia Statistics Agency, 2011; Mendelsohn et al., 2013) and it experiences extreme floods, as a result of extreme precipitation events (Persendt and Gomez, 2016; Persendt et al., 2015), which are socially and economically devastating (Mendelsohn et al., 2013). In 2009, for example, more than 670,000 people were directly affected by floods on the Namibian side alone, of which 21,000 were displaced (Government of Namibia, 2009). More than 900 small-and-medium business enterprises were closed and about 45,000 ha of cropland were destroyed (Government of Namibia, 2009). A total of 135 schools were forced to close and more than 20 roads were severely damaged, affecting accessibility to 12 health clinics (Government of Namibia, 2009). Some sewerage systems were washed away, leading sewage to mix with flood water (Government of Namibia, 2009). The mixing of surface water with sewage posed a high risk of water-borne diseases outbreak, especially given that a significant number of households still do not have access to clean water and therefore use open surface water for drinking (Namibia Statistics Agency, 2011). The overall economic damages caused by the 2009 floods in the CEB on the Namibian side were estimated at US$ 104.6 million. Extreme floods in the CEB do not only cause unacceptably high socio-economic impacts, they also lead to post-traumatic stress disorder amongst children (Taukeni et al., 2016) as well as high drowning casualties (Mendelsohn et al., 2013). Accurate and locally reliable baseline information on spatio-temporal dynamics of surface water in the CEB is urgently needed to support local spatial planning because human population is increasing rapidly in this basin, leading to high population density in flood-prone areas (Mendelsohn et al., 2013).

The main objective of this study was to produce long-term baseline information on surface water changes and dynamics for CEB and its surroundings (CEB + S) for supporting local spatial planning processes and for improving our understanding of the past surface water changes and dynamics in this human-inhabited endorheic basin. Long-term baseline information on surface water change and dynamic was generated from Landsat data (1990–2021) using a standard machine learning algorithm (Breiman, 2001). The following research questions were addressed:

a. How much of the area in the CEB + S has been inundated by surface water during 1990–2021?
b. How did the annual surface water extent change between 1990 and 2021? In which years did the CEB + S have the lowest and highest surface water extents?
c. Which areas are least and most frequently inundated in the CEB + S?
d. To what extent do publicly available Landsat-based global surface water products capture surface water extent in the CEB + S? How reliable are the available global surface water datasets regarding the spatio-temporal information on surface water changes and dynamics in the CEB + S?

These research questions were addressed by i) generating sample-based area estimates of surface water extent for thirty two years (1990–2021), ii) mapping and validating the maps for surface water extents, iii) quantifying long-term change in annual surface water extent, iv) characterising inundation frequency of surface water in CEB + S, and v) assessing the utility of globally available Landsat-based surface water maps (global products) for local surface water assessment by comparing them to the locally produced surface water product (local product). We defined surface water inundation as the presence of water on the earth surface as captured by a 30 m resolution Landsat imagery between 1990 and 2021, and surface water extent as the total area covered by surface water. Although the Landsat programme has been acquiring data since 1972, the paucity of data in our study area during the rainy season prior to 1990 was high, with some years having no single image during the wet season (October - April). Therefore, surface water mapping and analysis was limited to the period of 1990–2021 in this study.

2. Study area

Our study area (Fig. 1) covers the whole of the CEB (129368.8 km^2) and small parts of Kunene and Okavango basins (16500.8 km^2). The CEB is an ephemeral wetland, covering a portion of southern Angola and northern Namibia (Fig. 1). This trans-boundary deltaic drainage system deposits in the Etosha Pan, and is made up of inter-connected drainage networks locally known as *iishana (plural) or oshana (singular)*. The Etosha Pan is an endorheic depression located in the Etosha National Park, a flagship nature reserve for wildlife conservation in Namibia. The CEB is bordered by two perennial rivers, namely the Kunene and Okavango, which also drain the southern highlands of Angola (Fig. 1). The Kunene River deposits in the Atlantic Ocean whereas the Okavango River deposits in the Okavango Delta in Botswana, so, the Okavango Basin is also endorheic. Existing evidence shows that the Kunene River was also an endorheic system that once deposited in the Owambo Basin, before it got deflected towards the Atlantic Ocean (Hipondoka, 2005). Generally, the CEB is a flat area with elevation above sea level decreasing from 1500 m in southern Angola to 1080 m in the Etosha Pan. More than 1.3 million people live in the CEB, of which the majority are small-scale subsistence crop-livestock farmers (Namibia Statistics Agency, 2011; Mendelsohn et al., 2013). The Namibian side of the CEB is one of the most densely populated areas in Namibia, with population density reaching about 150 people per km^2 (Fig. 1A). Overall, about 42% of the Namibian population lives in the Cuvelai-Etosha Basin (Namibia Statistics Agency, 2011). Climatic conditions in the CEB are predominantly influenced by two high pressure systems, the South Atlantic Anticyclone and the Botswana Anticyclone (Mendelsohn et al.,

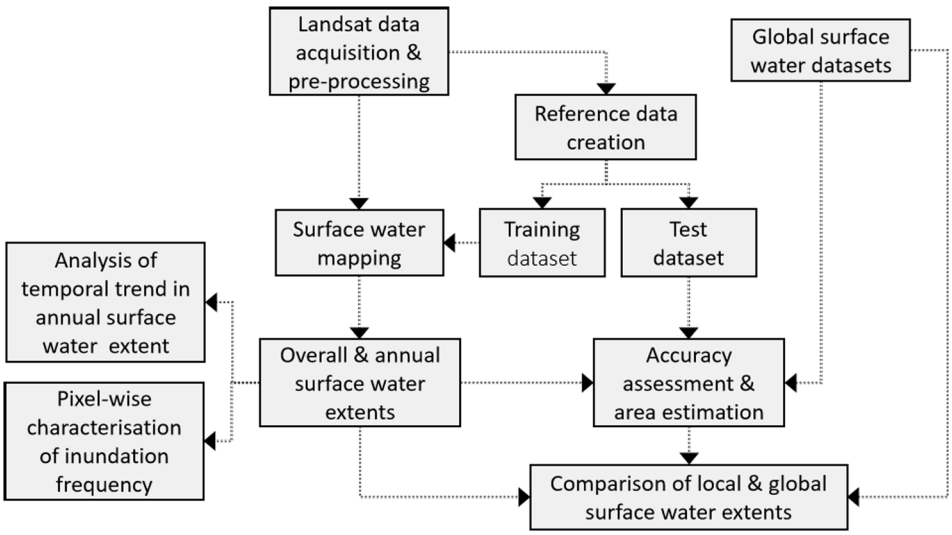

Fig. 3. The flowchart for mapping surface water inundation in the Cuvelai-Etosha Basin and its surroundings using Landsat data.

2013). These high pressure systems move southward during the summer (October–April; Fig. 2), allowing the inter-tropical convergence zone (ITCZ) with warm moist air to also move southwards (Mendelsohn et al., 2013). This southward movement of warm moist air triggers cloud development and subsequently precipitation over the Cuvelai-Etosha Basin. The average rainfall in the CEB has a strong east–west gradient on the Namibian side (Fig. 1B), whereby the extreme western areas receive an average annual rainfall of about 250 mm, whereas the extreme eastern areas receive an annual rainfall of about 600 mm (Fig. 1B). The wettest part of the Cuvelai-Etosha Basin in the Angolan highlands receives about 900 mm/year (Fig. 1B). Although the rainy season starts in September-November, significant rain is often not received until the January - April period (Fig. 2). During extreme flood events, *iishana* in the CEB become inundated with surface flood water, locally known as efundja, originating from upstream mainly from Angolan highlands and complemented by local rainfall, thus forming ephemeral wetlands. The flow of flood water downstream through the basin is generally slow due to the gentle sloping nature of the basin (Fig. 1C and D). Although *efundja* comes with many benefits for local inhabitants, which include fish (Hipondoka et al., 2018; Mendelsohn et al., 2013) and improved grass growth in iishana to support livestock grazing (Mendelsohn et al., 2013), extreme flooding in recent years have had devastating economic and social impacts in the CEB (Government of Namibia, 2009).

3. Data and methods

Several steps were followed to characterize surface water changes and dynamics in the CEB + S using Landsat data (Fig. 3). Landsat images (LT1 Tier 1) covering the study area were acquired and pre-processed (see Section 3.1). Then, reference pixels for training and validation purposes were selected (see Section 3.2) and labelled (see Section 3.3). Random forest models were then trained and subsequently applied to each Landsat image to compute the probability of surface water presence per pixel (see Section 3.4). Composite probability maps for surface water inundation were created (see Section 3.5), and the accuracy assessment of surface water maps including area estimates was then performed (see Section 3.6). Temporal change in annual surface water was quantified (see Section 3.7) and pixel-wise inundation frequency was characterised (see Section 3.8). Locally generated surface water maps were then compared to globally available Landsat-based surface water extent maps (see Section 3.9).

Table 1
The number of Tier1 Landsat images available at each Landsat scene (Row/Path) that covers the Cuvelai-Etosha Basin, from 1990 to 2021.

Landsat Scene (Row/Path)	Number of Tier 1 Landsat images	Average number of Landsat images per year
178,071	607	18
178,072	632	20
178,073	605	19
179,071	622	19
179,072	626	20
179,073	650	20
180,071	609	19
180,072	616	19
180,073	603	18

3.1. Landsat data acquisition and pre-processing

Surface water changes and dynamics in the CEB + S were mapped using all available analysis-ready Tier1 30 m resolution surface reflectance data from Landsat-5/TM, Landsat-7/ETM + and Landsat-8/OLI. We downloaded seven Landsat spectral bands (Blue, Green, Red, Near-infrared, Short-wave infrared 1 and 2, and Thermal infrared) and five corresponding spectral indices from The United States of America's Geological Survey (USGS) Landsat Surface Reflectance (SR) Climate Data Records (https://espa.cr.usgs.gov/). The downloaded spectral indices were: normalised difference vegetation index (NDVI, Rouse et al., 1973; Tucker, 1979), enhanced vegetation index (EVI, Liu and Huete, 1995), normalised difference moisture index (NDMI, Gao, 1996), soil-adjusted vegetation index (SAVI, Huete, 1988) and modified soil-adjusted vegetation index (MSAVI, Qi et al., 1994). In addition, we calculated the modified normalised difference water index (MNDWI, Xu, 2006). Tier 1 Landsat data have good geometric accuracy, and are thus suitable for time-series analysis. Surface reflectance data for Landsat-5/TM and Landsat-7/ETM + were generated using the standard Landsat Ecosystem Disturbance Adaptive Processing System (LEDAPS) algorithm (Masek et al., 2006; Schmidt et al., 2013), whereas Landsat 8 OLI surface reflectance products were generated using the Landsat-8/OLI surface reflectance algorithm (Vermote et al., 2016). Clouds and cloud shadows were masked in each Landsat image using pixel quality flags which were distributed together with Landsat surface reflectance data. Pixel quality flags were generated using the CFmask algorithm (Zhu et al., 2015; Zhu and Woodcock, 2012, 2014). A total of 5570 Landsat images spread over nine (9) Landsat scenes were used to map surface water changes and dynamics in the CEB + S, with the average number of

Table 2
The number of reference pixels which were used for training purposes and validation of surface water inundation maps. Training dataset was used to train the random forest model for surface water inundation, whereas the test dataset was used to validate the surface water inundation. Area proportion represents the size of each stratum.

MNDWI stratum	Training set	Test validation set	Area proportion
<−0.25	232	368	0.417
−0.25–0.00	251	199	0.460
0.01–0.24	183	144	0.040
0.25–0.49	175	175	0.018
0.50–0.74	182	167	0.022
>0.74	176	148	0.043
Total	1199	1201	1

Landsat images per scene per year varying from 18 to 20 images during the 1990–2021 period (Table 1).

3.2. Selection of reference pixels

Training data were needed to train the random forest algorithm for mapping surface water from satellite data, and validation data were needed for accuracy assessment and area estimation of surface water extents. Reference pixels were selected through stratified probability sampling (Midzuno, 1951; Stehman, 2009) to facilitate the creation of training and test validation data. To do this, a maximum-value composite image for MNDWI based on all available Tier 1 Landsat-5/TM and Landsat-8/ OLI MNDWI images covering the 1990–2021 period was first created for the whole study area using Google Earth Engine (Gorelick et al., 2017). The MNDWI image was classified into six classes (Table 2) based on the pixel values. Each class was treated as an independent stratum from which reference pixels were then selected using stratified probability sampling. In total, 2400 reference pixels were selected of which 1199 were for training purposes and 1201 for validation. (Table 2). For validation set, 385 samples were the ideal minimum sample size when aiming for 5% margin error and 95% confidence interval given the population size of 162,077,334 of 30 m Landsat pixels covering the study area. Our validation set of 1201 samples is therefore 3 times larger than the ideal minimum sample size.

3.3. Labelling of training and test validation samples

To validate our multi-year maps of surface water, we relied on visual interpretation of Landsat images themselves to create training and test validation data for surface water because there were no reliable and consistent multi-year in-situ observations or temporally consistent high spatial resolution satellite data covering the 1990–2021 period. Visual interpretation was done through a web application implemented on Google Earth Engine (https://github.com/jdbcode/ee-rgb-timeseries/blob/main/eo-timeseries-explorer.js) using a timesync approach (Cohen et al., 2010) which allows for interpretation of satellite image using visual clues (i.e. context, texture, shape and connectivity) in addition to temporal spectral response to determine the presence/ absence of surface water at each reference pixel. Fig. 4 shows the screenshot of the user-interface for the web application. The labeling of

Table 3
Landsat images from the wet and dry season in the Cuvelai-Etosha Basin on which the random forest models were trained to predict the probability of surface water presence.

	Wet season		Dry season	
Row/ path	Acquisition date	Sensor	Acquisition date	Sensor
178,071	1991-03-30	Landsat-5/ TM	1991-08-05	Landsat-5/ TM
178,072	1998-03-17	Landsat-5/ TM	1998-08-24	Landsat-5/ TM
178,073	2001-03-25	Landsat-5/ TM	2001-08-16	Landsat-5/ TM
179,071	1997-03-21	Landsat-5/ TM	1997-08-28	Landsat-5/ TM
179,072	2009-03-22	Landsat-5/ TM	2017-08-03	Landsat-8/ OLI
179,073	2017-02-24	Landsat-8/ OLI	2008-08-10	Landsat-5/ TM
180,071	2017-03-19	Landsat-8/ OLI	2017-08-10	Landsat-8/ OLI
180,072	2017-03-19	Landsat-8/ OLI	2017-08-10	Landsat-8/ OLI
180,073	2017-03-19	Landsat-8/ OLI	2017-08-10	Landsat-8/ OLI

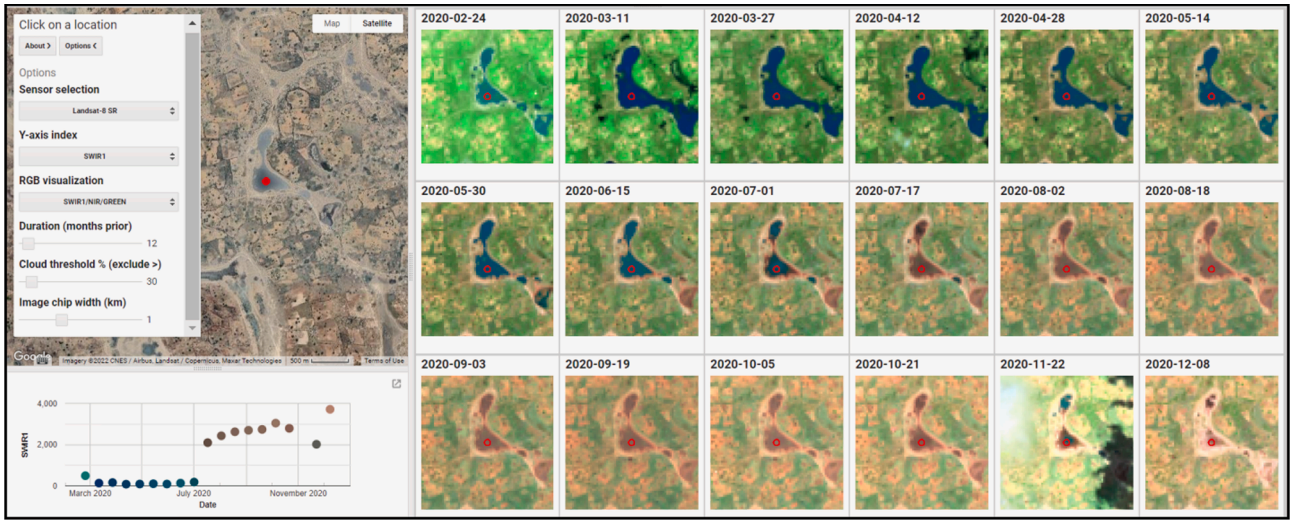

Fig. 4. A screenshot of the user-interface for web application, implemented on the Google Earth Engine, which was used for the interpretation of Landsat images to label surface water reference samples in the Cuvelai-Etosha Basin. The web application has three panels - the panel with high resolution Google Earth image background (top left panel), the pixel time series chart (bottom left panel), and the panel for image chips of Landsat multispectral images (right panel). In this example, the image chips are for Landsat-8/OLI visualised as SWIR1-NIR-GREEN colour composite. The original App is available at https://github.com/jdbcode/ee-rgb-timeseries/blob/main/eo-timeseries-explorer.js. (For interpretation of the references to colour in this figure legend, the reader is referred to the web version of this article.)

the training and test validation samples was done differently. For the training data, each sample was interpreted and labelled twice whereby one label was based on interpretation of an image from the wet season and the other from the dry season (see Table 3). Training the random forest models using data from the two seasons was necessary for minimising seasonal bias in the model predictions. Training samples were only interpreted from 18 multispectral images from Landsat 5/TM and Landsat-8/OLI comprising of nine images per season of which each image represent one of the nine (9) Landsat scenes covering the study area. In contrast to training samples, the test validation samples were elaborately interpreted and labelled through time resulting in each sample containing annual temporal information on the presence/absence of surface water for each year from 1990 to 2021. The presence/absence of surface water at each test validation sample per year was determined by visually inspecting all available Tier 1 multispectral Landsat surface reflectance images per year also using the web application (Fig. 4). For each year, a sample was assigned a "water" class if surface water was visible from at least one of the images from such a year, otherwise a "no water" class was assigned.

3.4. Surface water prediction

We computed the probability of surface water presence from Landsat data in the CEB + S using a random forest algorithm (Breiman, 2001) implemented in the *randomForest* R-package (Liaw and Wiener, 2002). The number of decision trees for the random forest model was set to 501 and the number of randomly selected candidate variables at each split was set to 5. The random forest algorithm is one of the widely used machine learning algorithm to map surface water from satellite images in recent years (e.g. Tulbure and Broich, 2013; Wang et al., 2018; Li and Xu, 2021). Random forest models, trained using the training data from wet and dry seasons to minimise seasonal bias (see Section 3.3), were used to predict the presence of surface water on each pixel for each Landsat image, resulting in an image time series of water presence probability. We used seven Landsat spectral bands (Blue, Green, Red, Near-infrared, Short-wave infrared 1 and 2, and Thermal infrared) and six spectral indices (NDVI, EVI, NDMI, MNDWI, SAVI, MSAVI) as predictors for surface water presence. Data analysis was performed in R (R Core Team 2018) with raster data handling capabilities powered by *raster* R-Package (Hijmans and van Etten, 2015) and *rgdal* R-package (Bivand et al., 2018).

3.5. Creating composite probability maps for surface water

We created overall and annual composite probability maps for surface water. An overall probability map was created from all available individual probability maps (see Section 3.4) using maximum-value composite approach. This approach was used to ensure that each pixel in the composite probability map contains the highest temporal probability value for surface water. Annual probability maps were created from individual probability maps of surface water for each year also using maximum-value composite approach.

3.6. Accuracy assessment of surface water maps

The accuracies of the overall and annual surface water maps were assessed using the test validation data set (Table 2) based on the recommended good practice for accuracy assessment and area estimation (Olofsson et al., 2014; Stehman, 2012). Our goal was to generate overall annual surface water maps that have the lowest area bias (the lowest difference between producer's and user's accuracy). So, we used probability thresholds that minimise area bias to bin overall and annual probability maps into water / no water classes. Monthly surface water maps for each year were created by applying probability thresholds which were used to create corresponding annual surface water maps. The probability threshold for annual surface water maps were higher than 0.8, except for two years (1990 and 1996) when thresholds were 0.79 and 0.70, respectively. The probability threshold for the overall local water extent was 0.95. During accuracy assessment, an error matrix populated by estimated proportions of area based on sample count weighted against the area proportion of the strata was constructed to facilitate the calculation of accuracy metrics for surface water maps. Table 4 shows a generic population error matrix for water and no water with cell entries expressed in terms of area proportions. From the error matrix, the user's and producer's accuracies were calculated as user's accuracy = $p_{ii}/p_{i.}$ and producer's accuracy = $p_{ii}/p_{.i}$ where p_{ii} is an area-adjusted proportion for reference pixels with surface water that was correctly mapped; $p_{i.}$ is the total mapped area proportion for surface water; and $p_{.i}$ is the total estimated area proportion for surface water based on reference data. The 95% confidence intervals for user's and producer's accuracies were estimated as ± 1.96 , where is the variance for a respective accuracy metric (Olofsson et al., 2013, 2014). The variance for each accuracy metric was calculated following the formulas proposed in Olofsson et al. (2014). We calculated the mapped and estimated areas for overall and annual surface water extents. The mapped (M_a) and estimated (E_a) areas of surface water, expressed in km^2, were calculated as $M_a = z_{pixel} \times 0.0009$ and $E_a = p_{.i} \times T_{pixel} \times 0.0009$ respectively, where z_{pixel} is total number of pixels classified as water, and T_{pixel} is the total number of Landsat pixels that covered the study area. The estimated water extent refers to the total area of surface water based on sample estimates, whereas the mapped extent refers to the total area of surface water based on the total pixels classified as water. The 95% confidence interval for estimated surface water extent was calculated following Olofsson et al. (2014) approach, where the 5% margin of error for the confidence interval is estimated as $\pm 1.96 \times T_{pixel} \times S(P_{.i})$. In this case, the $S(P_{.i})$ is the standard error for sample-based area estimates, calculated as $S(P_{.i}) = \sqrt{[((p_{i.}p_{ii} - p_{ii}^2)/(n_{i.} - 1)) + ((p_{j.}p_{ji} - p_{ji}{}^2)/(n_{j.} - 1))]}$, where $n_{i.}$ and $n_{j.}$ are row totals for sample counts.

Table 4
A generic population error matrix for water and non-water where cell entries are expressed in terms of proportion of area.

		Reference		
		Water	Non-water	Total
Map	Water	p_{ii}	p_{ij}	$p_{i.}$
	Non-water	p_{ji}	p_{jj}	$p_{j.}$
	Total	$p_{.i}$	$p_{.j}$	1

3.7. Quantifying temporal trend in annual surface water extent

We quantified the long-term temporal trend in annual surface water extent and mean rainfall in the CEB + S using a linear model to understand how the annual surface water extent changed between 1990 and 2021. We also correlated the annual surface water extent with the mean rainfall using Spearman correlation to understand how annual surface water extent in the CEB + S is related to the prevailing rainfall.

3.8. Characterising pixel-wise inundation frequency

We characterised pixel-wise inundation frequency in the CEB + S to

Table 5
Inundation frequency (years) categories which were used for classifying the inundated areas in the Cuvelai-Etosha Basin and its surroundings.

Inundation frequency score	Inundation frequency	Assigned class name
<0.26	1 to 8	Rarely inundated
0.26–0.50	9 to 16	Occasionally inundated
0.51–0.75	17 to 24	Frequently inundated
>0.75	25 to 32	Very frequently inundated

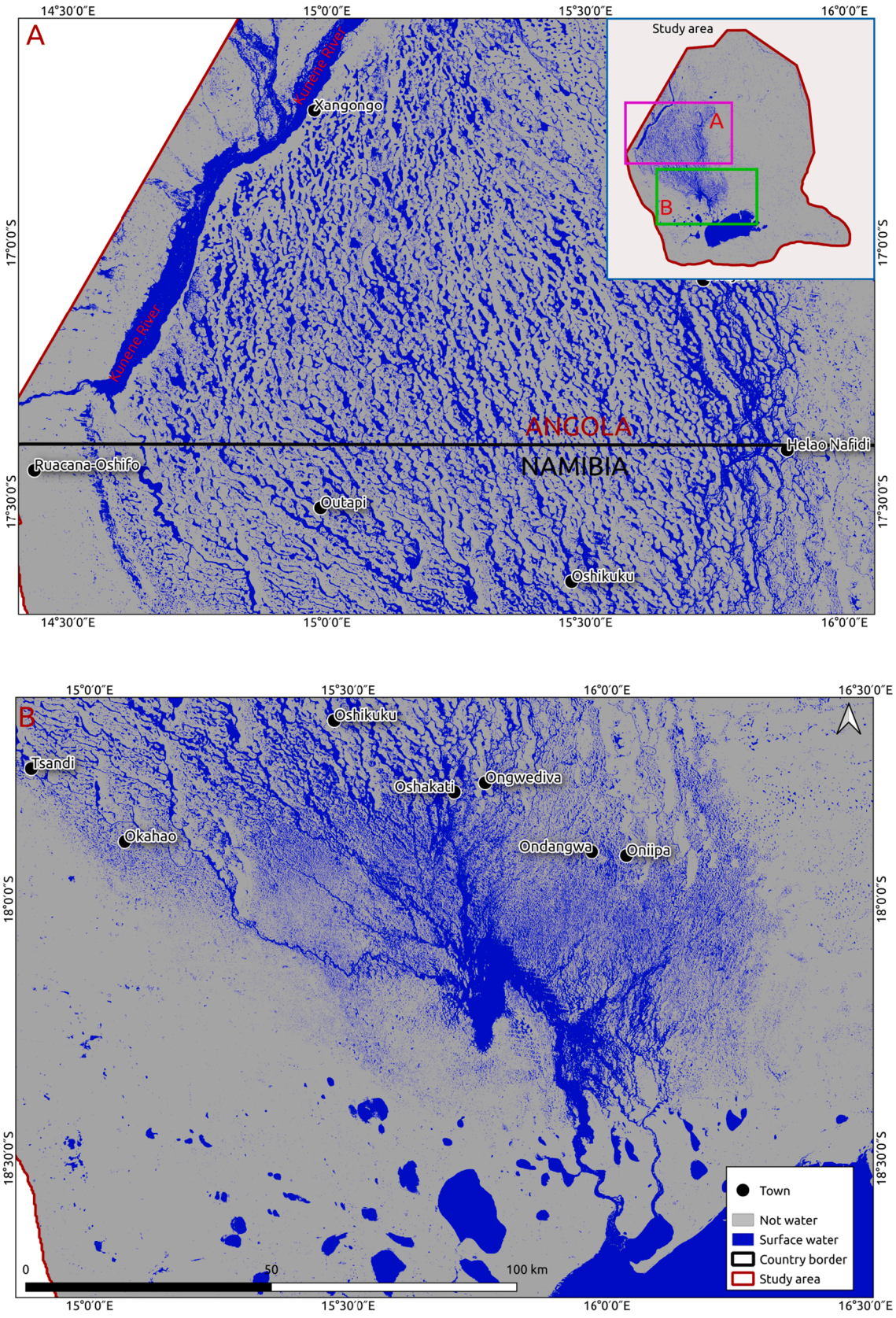

Fig. 5. Landsat-based overall surface water extent for CEB and its surroundings as mapped by the local product during the 1990–2021 period.

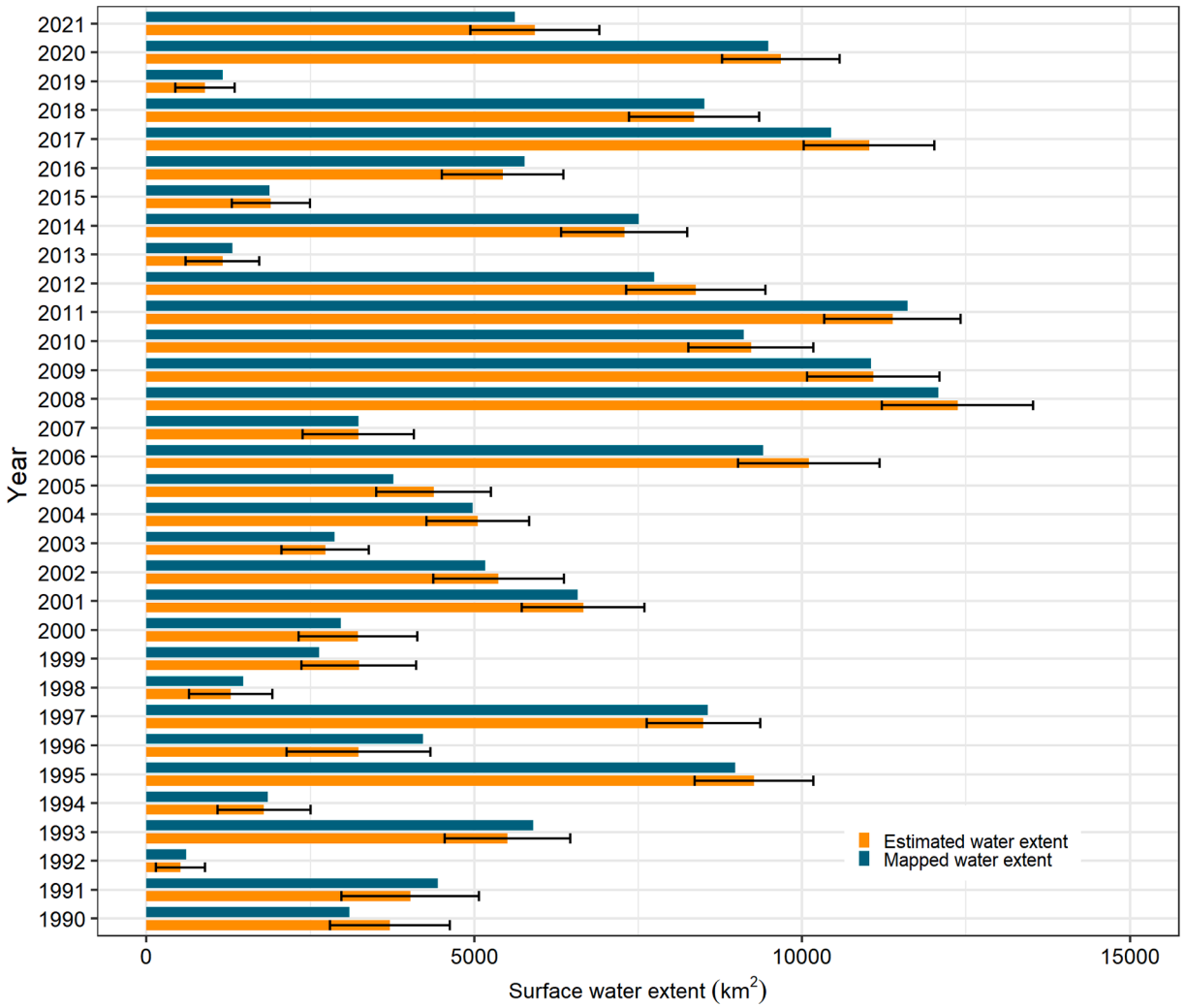

Fig. 6. Annual estimated (sample-based) and mapped surface water extents derived in the CEB + S for 1990–2021 period. The mapped water extents were derived from from Landsat data. The standard error bars represent the 95% confidence interval.

allow the identification of most and least inundated areas, which can be used to identify critical water bodies. We quantified inundation frequency by counting the number of years between 1990 and 2021 when surface water was detected on each pixel from Landsat data. A pixel-wise inundation frequency score (IFS) was then calculated as IFS = w/T_E, where w is the inundation frequency and T_E is the temporal extent for the study, which was 32 years. We then classified the inundated areas into four classes based on the IFS (Table 5).

3.9. Comparison to global surface water products

Publicly available global surface water datasets (e.g. Pekel et al., 2016; Pickens et al., 2020) generated from Landsat data have become alternative data-source for local planning and surface water monitoring activities in areas where locally accurate maps of surface water do not exist. But the local utility of these datasets for local surface water assessment and monitoring remains unknown. To assess their suitability, we used statistically robust sample-based approach to compare estimates of surface water extents to the mapped water extents from our local maps (local product) and two global surface water products, namely European Commission's Joint Research Centre (JRC) global surface water (JRC product, Pekel et al., 2016) and the Global Land Analysis and Discovery (GLAD) global surface water (GLAD product, Pickens et al., 2020). The two global surface water products were all generated from the same Landsat data and provide overall, annual and monthly information on the extent of surface water across the globe. The JRC product was available from 1984 to 2020, whereas the GLAD product was only available from 1999 to 2021. For the overall surface water extent, the comparison was only done for local and JRC products because the GLAD product had a shorter temporal extent (1999–2021). Global products were cropped to match the spatial extent of the local product. Area estimates and spatial accuracy (user's and producer's) for the global and local products were assessed using the same reference data (see Section 3.2).

4. Results

4.1. Overall surface water extent

Sample-based area estimates show that 15676.98 ± 1079.98 km^2, equivalent to 10.6% of the study area, have been inundated with surface water in the CEB + S between 1990 and 2021. This overall inundation extent was mapped within the error-margin by the local surface water product (mapped area = 16273.48 km^2). The overall surface water extent (Fig. 5) was mapped with high user's (91.5 ± 2.5%) and producer's (91.1 ± 6%) accuracies. The commission and omission errors were less than 10% and the area bias was less than 0.5% in favour of the commission error. Our analysis shows that 90.2% of the overall surface water extent mapped by the local product in the study area was within the CEB, and the remaining 9.8% was detected in the surrounding areas

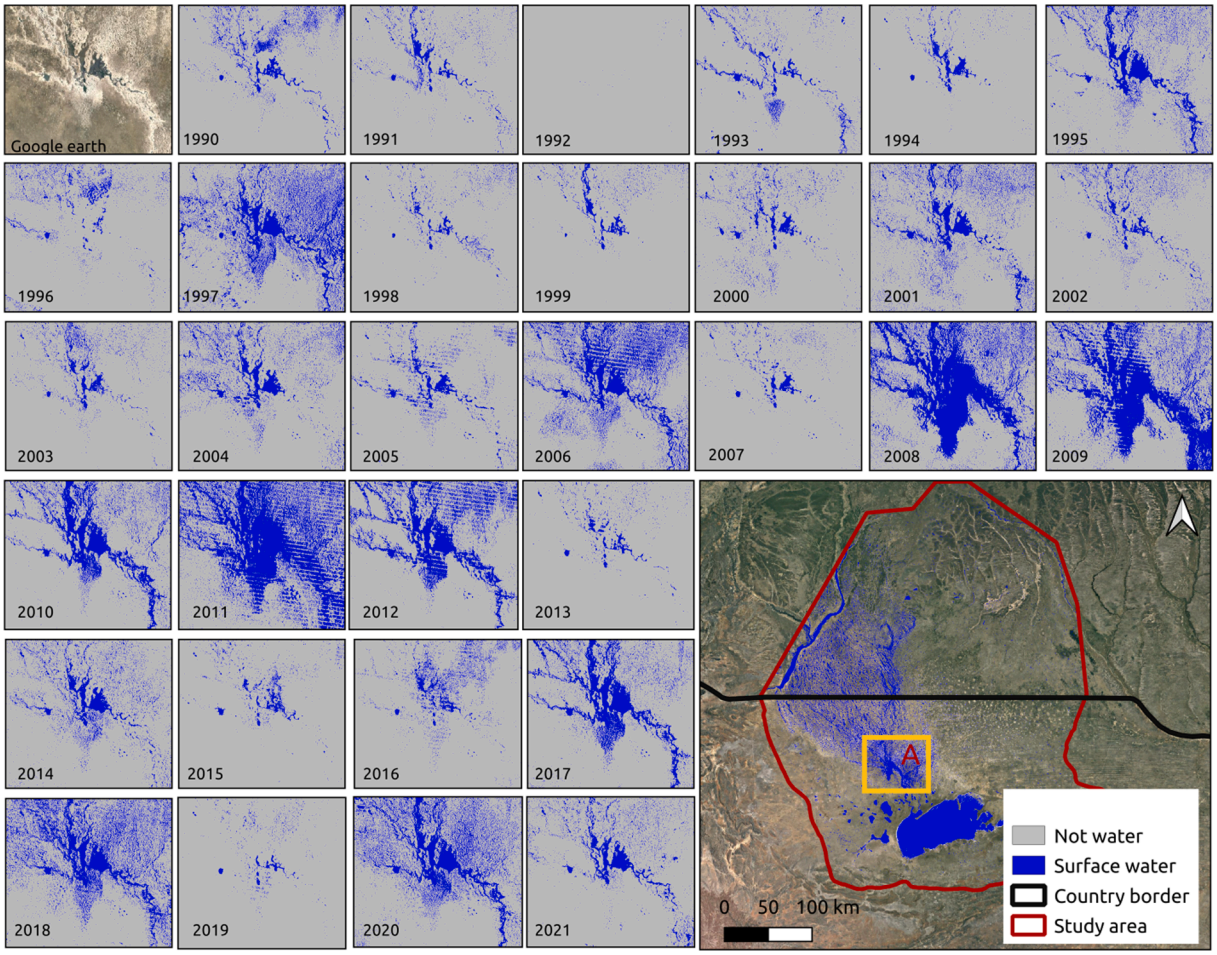

Fig. 7. Change in annual surface water extent during 1990–2021 period at Omadhiya Lakes where surface water converges before flowing towards Etosha Pan. The background high resolution multi-spectral image is from Google Earth™. The striping effect in water extent for 2006, 2009, 2011 and 2012 is caused Landsat 7 SLC-off gaps.

that cover the Kunene and Okavango basins.

4.2. Annual surface water extent

Annual sample-based area estimates show a high interannual variability in surface water extent in the CEB + S between 1990 and 2021, with surface water extent ranging from 520.8 ± 375.7 km^2 to 12372.3 ± 1154.7 km^2. The lowest extent was recorded in 1992 whereas the highest extent of surface water was recorded in 2008. From the surface hydrology perspective, 1992 and 2019 were the driest years in CEB + S during 1990–2021 period, with surface water extent of less than 1000 km^2, whereas 2006, 2008, 2009, 2011 and 2017 were the wettest years with annual surface extent exceeding 10,000 km^2. The annual surface water extents were generally mapped accurately by the local extent, with mapped water extents within the error margin for sample-based estimates (Fig. 6). A spatial depiction of interannual change in surface water extent at Omadhiya Lakes where surface water converges before flowing towards Etosha Pan is shown in Fig. 7.

The user's and producer's accuracies for mapped annual surface water extents varied greatly, but the surface water extent for many years was mapped with high user's and producer's accuracies (Table 6). Out of 32 annual surface water maps, 72% had both user's and producer's accuracy higher than 60% (Table 6). Surface water maps for 1996 and 1998 had the lowest accuracy, where both the user's and producer's accuracy were lower than 45% (Table 6), which indicates that the commission and omission errors for these maps were excessively high. The most important predictors of surface water were water indices (MNDWI, NDMI) and SWIR bands, whereas the bands from visible spectral regions were the least important (Fig. 8).

4.3. Trend in annual surface water extent

Trend analysis did not reveal a significant increase in annual surface water extent (Fig. 9A) in the CEB + S during 1990–2021 period (df = 30, p = 0.0685). The mean rainfall also did not show a siginificant change over the last 32 years (df = 30, p = 0.6544). In the late 2000 s, the CEB + S was characterised by successive years (2006, 2008, 2009, 2010, 2011) with above average rainfall, a pattern which was rare during 1990–2021 period (Fig. 9C). The Spearman correlation between the annual surface water extent and mean rainfall was 0.66 (Fig. 9B).

4.4. Inundation frequency

Over 40% of the area inundated in the CEB + S during 1990–2021 was rarely inundated, and less than 5% (4.2 km^2) was inundated very frequently during the same time period, of which 76% (3.3 km^2) was in the CEB (Fig. 10A). Rarely inundated areas are areas that were inundated less than 9 times during the entire 1990–2021 period, whereas very frequently inundated areas were inundated more than 24 times during the same study period. A significant portion (>12%) of the inundated area was inundated only once during 1990–2021 (Fig. 10B) in the whole study area (CEB + S). Very frequently inundated area were mainly portions of the perennial Kunene which was part of our study area and the Olushandja Dam (Fig. 11A), as well as the Omadhiya Lakes

Table 6
Overall, and producer's and user's accuracies for annual surface water extents derived from Landsat data over CEB + S. The standard errors represent the 95% confidence interval.

Year	PA [%]	UA [%]	OA [%]
1990	64.3 ± 15	62.1 ± 10	98.2 ± 0.6
1991	53.8 ± 14	53.7 ± 09	97.6 ± 0.7
1992	50.8 ± 36	52.2 ± 24	99.7 ± 0.2
1993	74.1 ± 12	73.3 ± 06	98.1 ± 0.6
1994	50.1 ± 20	51.7 ± 14	98.9 ± 0.5
1995	87.5 ± 08	87.2 ± 04	98.5 ± 0.6
1996	33.2 ± 13	32.5 ± 11	97.1 ± 0.7
1997	87.3 ± 08	87.8 ± 04	98.6 ± 0.6
1998	42.5 ± 22	42.6 ± 15	99.0 ± 0.4
1999	59.8 ± 16	60.4 ± 09	98.3 ± 0.6
2000	56.5 ± 15	57.9 ± 10	98.2 ± 0.6
2001	80.3 ± 10	79.1 ± 06	98.2 ± 0.6
2002	70.5 ± 12	70.9 ± 07	97.9 ± 0.7
2003	79.9 ± 17	70.5 ± 08	99.0 ± 0.4
2004	81.5 ± 11	79.5 ± 06	98.7 ± 0.5
2005	71.7 ± 13	73.1 ± 08	98.4 ± 0.6
2006	83.7 ± 08	85.1 ± 04	98.0 ± 0.7
2007	63.0 ± 16	62.4 ± 09	98.4 ± 0.6
2008	85.8 ± 07	85.9 ± 03	97.7 ± 0.8
2009	87.3 ± 07	88.8 ± 03	98.3 ± 0.7
2010	86.4 ± 08	84.1 ± 04	98.2 ± 0.6
2011	87.6 ± 07	86.0 ± 04	98.0 ± 0.7
2012	80.7 ± 09	78.5 ± 05	97.7 ± 0.7
2013	53.4 ± 25	46.5 ± 16	99.2 ± 0.4
2014	80.9 ± 10	81.2 ± 05	98.2 ± 0.6
2015	67.4 ± 20	71.2 ± 11	99.3 ± 0.4
2016	75.2 ± 12	75.1 ± 07	98.2 ± 0.6
2017	88.3 ± 07	86.1 ± 04	98.1 ± 0.7
2018	82.5 ± 09	84.4 ± 04	98.2 ± 0.7
2019	62.7 ± 30	49.3 ± 18	99.4 ± 0.3
2020	88.6 ± 07	87.0 ± 04	98.4 ± 0.6
2021	75.0 ± 11	74.2 ± 07	98.0 ± 0.6

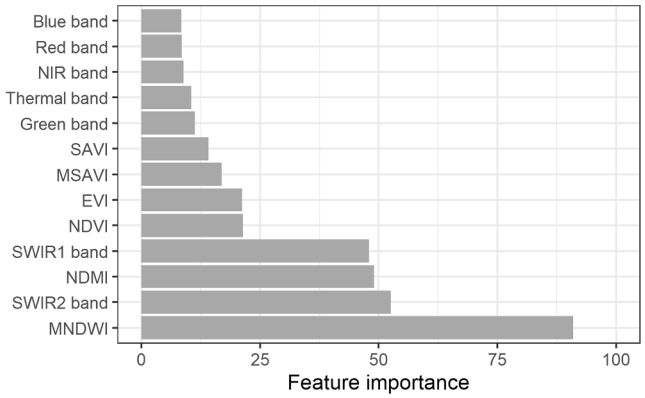

Fig. 8. Random forest feature importance for surface water mapping Cuvelai-Etosha Basin with Landsat. Metrics with high feature importance were the most important predictors of surface water.

and parts of several *iishana* in the CEB (Fig. 11B). Very frequently inundated areas therefore represent areas which often had surface water even during dry years, whereas rarely inundated areas correspond to areas which become inundated only during extreme floods. In some frequently inundated areas, surface water has ceased to occur (Fig. 12D) whereas previously uninundated areas are now frequently inundated (Fig. 11E).

4.5. Local and global surface water extents comparison

Variation in the annual surface water extent was accurately captured by the local product (Fig. 13), leading to the Spearman correlation of 0.99 between the mapped and estimated extents. For the GLAD product, the correlation between the mapped and estimated annual water extents was also high 0.92. However, the GLAD product underestimated surface water extent almost for each year (Fig. 13). The correlation between the estimated water extent and water extent mapped by JRC product was 0.60. The JRC product also underestimated the extent for most of the years (Fig. 13). The overall water extent mapped by the JRC product (5618.02 km^2) in the CEB + S was at least two times lower than the sample-based area estimates (15677 ± 1080 km^2). Based on sample estimates, the highest annual water extent (12372.3 ± 1154.7 km^2) was recorded in 2008. This water extents was much higher than the extent mapped by JRC product (4280.64 km^2) and GLAD product (7568.25 km^2). The water extent mapped by local product (12076.25 km^2) in the same year was much closer to the one estimated from reference data. Fig. 14 shows spatial comparison of the local and global surface water maps at three sites in the CEB for March 2017. Generally, the GLAD surface water extents for CEB + S are more realistic than JRC surface water extents (Fig. 13), but both global products do not provide reliable extent of surface water inundation in this basin.

5. Discussion

This paper estimated and mapped surface water extents in the CEB + S for 32 years (1990–2021) to improve our understanding of changes and dynamics of surface water in this human-inhabited endorheic basin and to provide the first most accurate spatio-temporal information on the surface water changes and dynamics in the CEB at 30 m resolution. Sample-based area estimates show that 10% of the CEB + S has been inundated by surface water between 1990 and 2021 though the maximum area inundated in a single year was only 8%. This could be due to the fact that some areas have experienced inundation cessation and inception over the years as a result of human-induced land modifications (see Fig. 12). We found a high interannual variability in surface water extents in the CEB + S, with surface water extent less than 0.5% of the study area during drier years, and about 8% during the wet years. This interannual variability could even have been much higher if small parts of the perennial Kunene and Okavango Rivers were not included in the study area. Higher interannual variability in the annual water extents is a result of extreme droughts and floods that occurred in the CEB + S during the 1990–2021, and also due to high evaporation. Even if an extreme floods occur in the CEB + S, most of the surface water evaporated in few months. Interannual variability in the surface water extent has been observed in other water basins in drylands (Tulbure and Broich, 2013), but the variability in those areas were less strong because of large perennial rivers that transverse such basins. During the thirty two years (1990–2021), the 2008–2011 period was the wettest in the CEB + S resulting in larger surface water extents. This period was characterized by extreme floods in the CEB which were the most socially and economically devastating floods in recent decades in this area (Mendelsohn et al., 2013). Our area estimates show that the surface water extents for 1992, 1998, 2013 and 2019 were the smallest during 1990–2021 period. This is not surprising because these years were characterized by extreme droughts which have had devastating impacts on livestock and livelihood of many inhabitants in Namibia, including in the CEB (Mendelsohn et al., 2013; Sweet, 1998). We did not find significant trend in annual surface water extent and rainfall in the CEB + S during the 1990–2021 period. The correlation between the annual surface water extent and mean rainfall was moderate. This is probably because, or some years with relatively high rainfall, the rain might have been spread over many days with longer temporal gap between rainfall events. Such rainfall pattern may not trigger flooding due to high evaporation rate in the study areas.

The overall surface water extent for 1990–2021 period was mapped with user's and producer's accuracies over 90%. These accuracies are similar to those achieved by Tulbure et al. (2016) who mapped surface water extent over the Murray–Darling Basin in Australia during 1986–2011 using Landsat data. The overall surface water extent

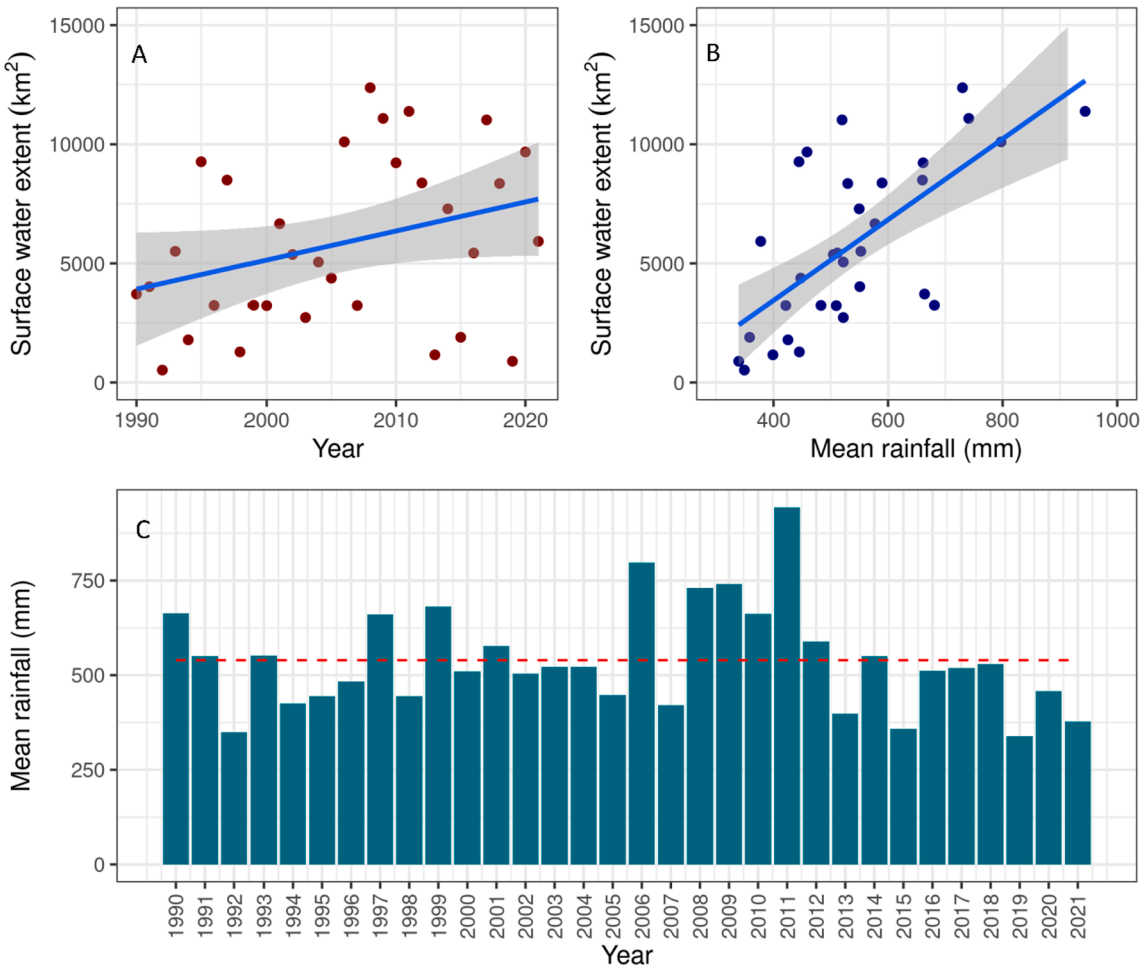

Fig. 9. Trends in annual surface water extent (A), the relationship between surface water extent and mean rainfall (B) and temporal distribution of mean rainfall in the Cuvelai-Etosha Basins and its surroundings (C) during 1990–2021 period. The red dashed line C indicates the long-term temporal mean of the rainfall. Rainfall data are based on the CHIRPS gridded rainfall estimates (Funk et al., 2014), and were averaged spatially. (For interpretation of the references to colour in this figure legend, the reader is referred to the web version of this article.)

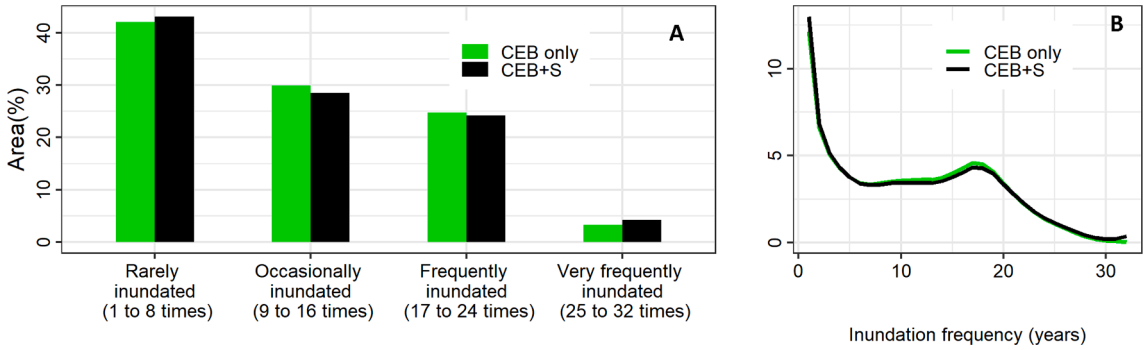

Fig. 10. Distribution of area by inundation frequency category (A) and by number of frequency (B) in the Cuvelai-Etosha Basin and its surrounding area during 1990–2021 period.

produced in this study provides the first most accurate and reliable overall surface water extent for CEB + S, and could therefore play an important role in other applications such as surface hydrological modelling, which often require input from remote sensing data (Heimhuber et al., 2016), to explore future flood risk under various climatic scenarios. This multi-decadal water extent can also be used as a benchmark mask when monitoring surface water evolution during extreme floods, and can play a critical role in spatial planning processes in the basin to minimise inappropriate land modifications and human settlement expansions.

Extracting drainage network for CEB from the best available digital elevation models (with 30 m horizontal and 5 m vertical resolutions, Takaku et al., 2018) is challenging (Niipele and Chen, 2019; Persendt and Gomez, 2016) because the CEB is generally flat. As a result, accurate dataset for drainage networks does not exist to support surface hydrology studies in the basin. Such drainage networks can be inferred from this multi-decade surface water extent to improve our understanding of the drainage networks inter-connectedness in the basin. Identifying the

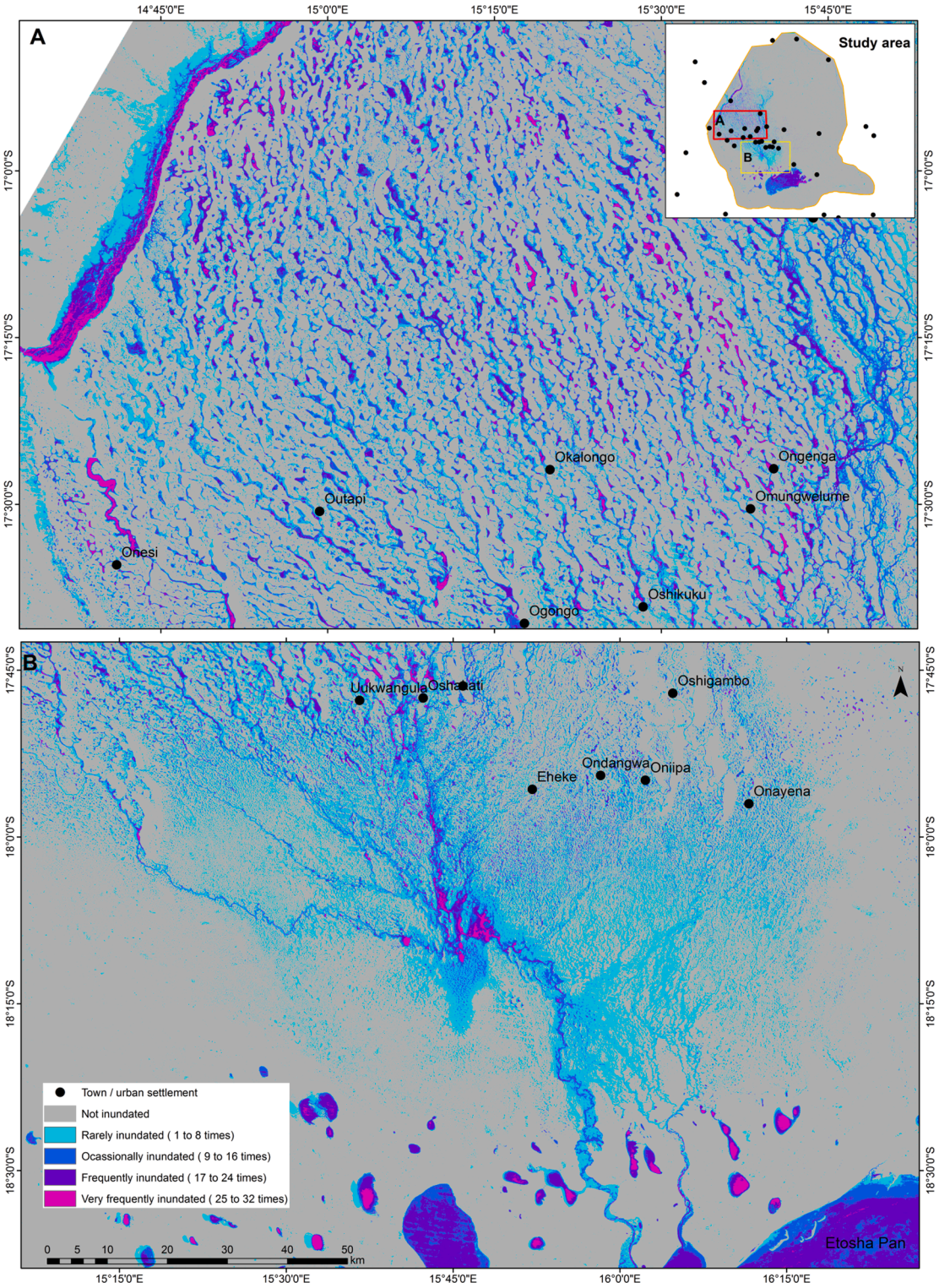

Fig. 11. Spatial patterns of inundation frequency in the CEB + S during 1990–2021 period.

inter-connectedness of critical drainage network would allow us to determine water channels that should be protected from land transformations to maintain the integrity of surface water flow in the CEB. Inferred drainage networks would also be needed for studies that aim to identify critical routes of seasonal fish and fisheries refugia in the CEB (e.g. Hipondoka et al., 2018).

When compared to area estimates based on reference data, our maps for annual surface water extent captured the interannual variability in surface water extent for CEB + S accurately, except that some maps of much drier years had higher omission and commission errors. High omission and commission errors for drier years imply that our random forest models were unable to separate correctly water pixels from non-water pixels during drier years, probably because of high surface reflectivity and shallowness of the water bodies. Our result of low user's and producer's accuracies during dry years is different from the findings of Tulbure and Broich (2013) who also used random forest model to map

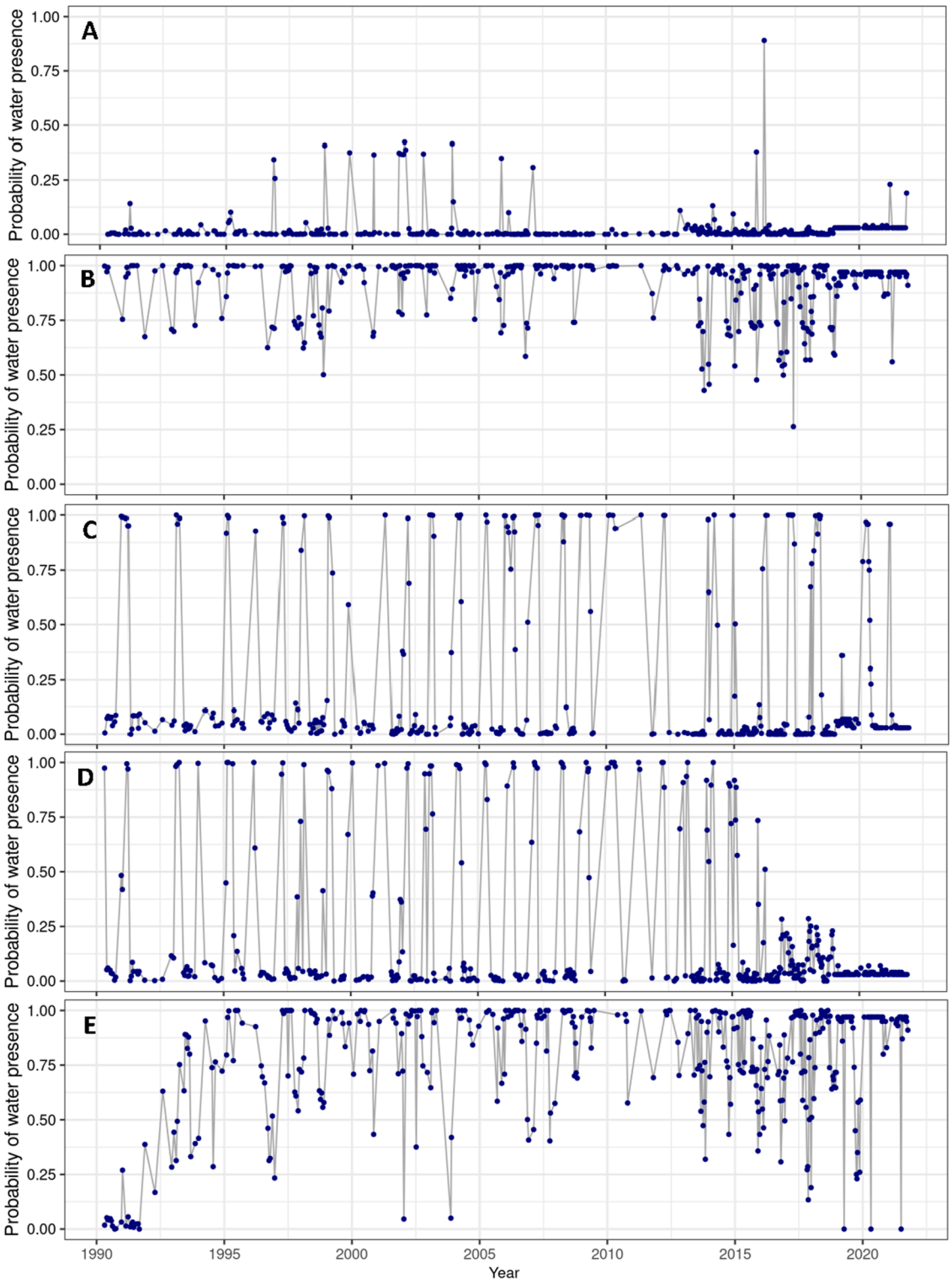

Fig. 12. The full pixel-time series for probability of water presence, with high values indicating high likelihood of water presence on a pixel. (A) inundation occurs only over few events (crop field: 17.6798S, 15.2459E), (B) almost permanently inundated area (lake: 17.6728S, 15.2926E), (C) inundation occurs in many years but dries up during the dry season (oshana: 17.5672S, 15.6664E), (D) seasonal inundation has ceased in 2015 due to land grading in Okalongo settlement (17.4466S, 15.3273E) to construct buildings, and (E) inundation emerged in 1994 from a gravel pit excavated for material to construct a road between Endola and Oshakati (17.6675S, 15.7232E). The probability of water presence time series was derived from all cloud-free Landsat observations from 1990 to 2021 using a random forest model.

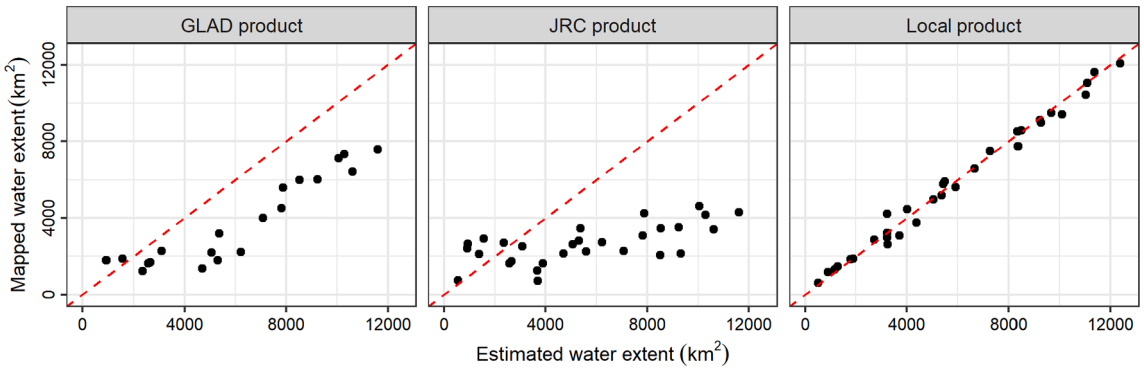

Fig. 13. Relationship between annual estimated and mapped surface water extents for GLAD, JRC and local products in the CEB + S. Annual surface water extents were estimated/mapped between 1990 and 2021 period. Mapped areas were derived from Landsat data. Estimated extents were based on sample reference data.

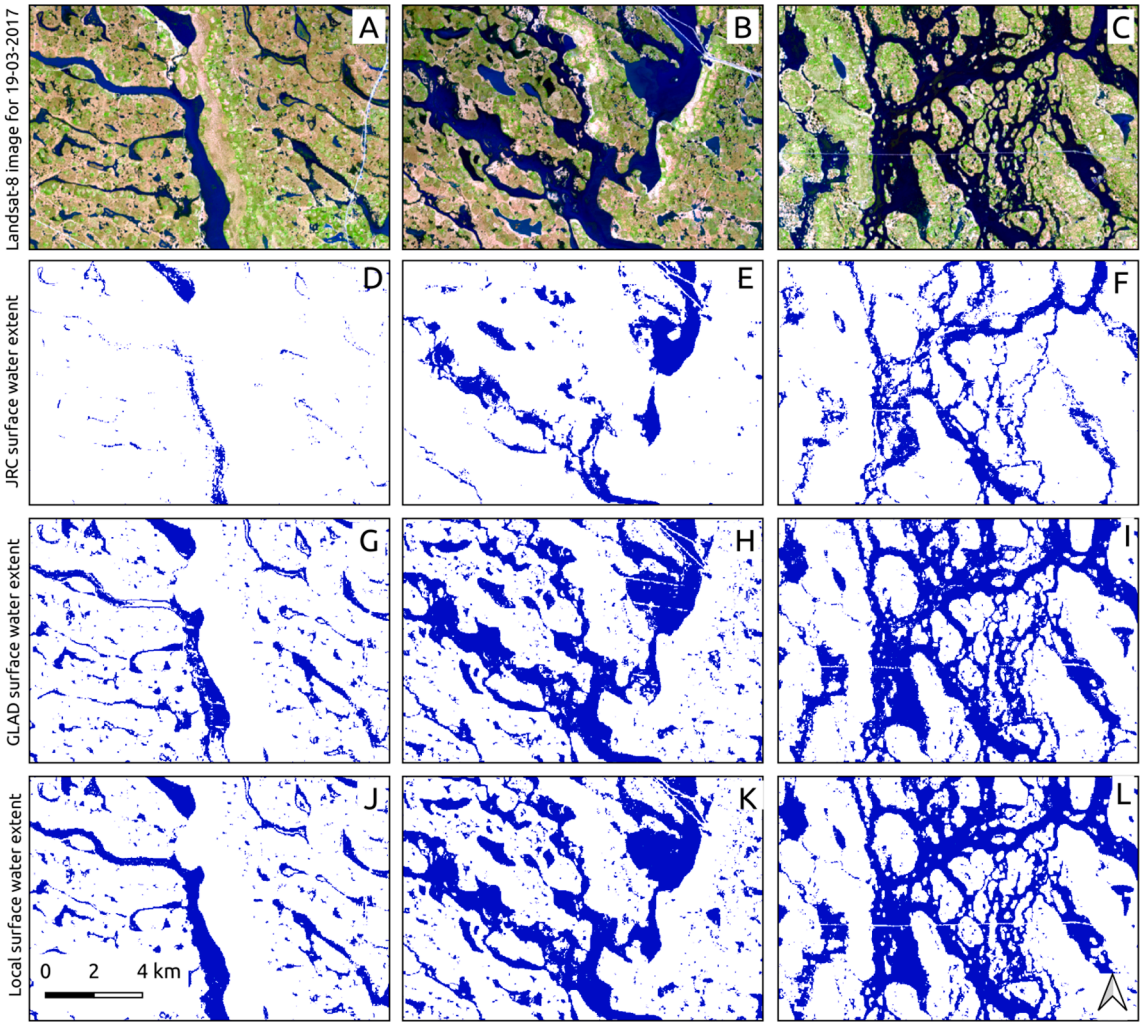

Fig. 14. Spatial comparison of local and global surface water products at three sites (A: 17.646S, 14.856E; B: 17.633S, 15.138E; C: 17.440S, 15.793E) in the CEB for March 2017. The multi-spectral images (A-C) visualised as 5–4-3 colour composite show surface water as captured by Landsat-8/OLI on 19 March 2017 and is compared against the surface water extent generated by JRC product (D-F), GLAD product (G-I) and local product (J-L) from the same image. Note that this was the only image available for March 2017.

surface water in Murray–Darling Basin of Australia from Landsat data. Tulbure and Broich (2013) reported lower producer's and user's accuracies of water extent for wet years than dry years. This difference might be due to the way we trained our random forest models, and the geomorphological differences between the two basins. However, Tulbure and Broich (2013) had separate models for various seasons whereas we used one random forest model trained using data from wet and dry seasons. Our relatively small training dataset (n = 1199) might also have contributed to low mapping accuracy during dry years. Future studies on surface water mapping in the CEB + S or similar setting should therefore consider using a significantly large representative training dataset to improve surface water mapping accuracy.

Continuous availability of surface water bodies in any landscape is important because such water bodies support many important biological and ecological processes (Allen et al., 2020). In the CEB + S, however, only 4% of the total inundated area had water almost every year during 1990–2021 period, and this area could be much smaller if the portions for perennial Kunene and Okavango rivers are excluded. Our analysis did not include identification of non-river bodies which retain water throughout the year, including during dry years. However, areas that retain or accumulate water during dry years in drylands provide important ecosystem services, and should therefore be identified in future studies to allow for protection from land transformations and pollution. In the context of CEB, identifying non-river bodies which retain water throughout the year would also be critical for the ongoing research which is investigating the main sources of seasonal fish that become prevalent in *iishana* during good rain seasons (Hipondoka et al., 2018; Mendelsohn et al., 2013).

A large portion (>40%) of the area that was inundated in the CEB during 1990–2021 was rarely inundated. With population still growing in the CEB + S, rarely inundated areas could become prime target for land transformation to accommodate human settlements and economic activities. Such land transformations, however, could lead to massive socio-economic impacts during extreme floods if no preventive measures are put in place. Therefore, our surface water maps provide necessary spatio-temporal information that could inform future land transformation activities in the CEB to minimise negative socio-economic impacts during extreme floods.

Global datasets for surface water are seen as potential alternative sources of spatio-temporal information for the areas where locally produced accurate maps for surface water do not exist. Our analysis, however, shows that globally available Landsat-based maps for surface water extent (Pekel et al., 2016; Pickens et al., 2020) underestimate surface water extent in the CEB + S. They even fail to correctly capture interannual variability in surface water in this basin. However, the GLAD product performed reasonably much better than the JRC product. The inability for globally generated surface water products to properly map surface water extent in the CEB + S is not surprising because global products were generated using globally tuned algorithms, and would not be able to capture complex local variability in surface water conditions. Further refinement of algorithms through increased training data from regions with complex surface water dynamics could potentially improve the accuracy of global surface water products.

Overall, this study provides the first most accurate baseline information on surface water changes and dynamics over three decades, and this information can support surface water management and landscape transformation policy formulation for CEB to minimise flood-related economic losses in the future. However, there are a few limitations to this dataset. Firstly, the overall and annual surface water estimates and maps undoubtedly underestimated the surface water extent in the CEB + S. This is because inundation caused by flash flood which have shorter residency period might have been missed because Landsat has temporal revisit of 16 days when only a single sensor is in orbit or 8 days when two Landsat sensors are in orbit. When this temporal revisit is coupled with cloud cover, most of the surface water might have evaporated or seeped into the soil before it could be captured by Landsat. With ongoing effort to harmonise data from Landsat and Sentinel-2 sensors (Claverie et al., 2018; Shao et al., 2019), the problem of low revisit time will be addressed. The benefit of using harmonised Landsat and Sentinel-2 dataset for surface water mapping has been demonstrated recently (Tulbure et al., 2022a). Secondly, water bodies smaller than 0.09 ha were possibly not mapped accurately by 30 m resolution Landsat data due to mixed pixel problems, and very shallow water might not have been detected, especially given that we relied on visual interpretation of 30 m resolution Landsat imagery for reference data. A typical example of water bodies missed by our product is the 160 km man-made open water canal with width smaller than 5 m that supply bulk water throughout the year from Calueque dam in Angola to Oshakati in Namibia for irrigation and domestic use. Mapping water bodies of this size accurately would therefore require satellite data with much higher spatial resolution. Data from the European Copernicus satellites with 10 m and PlanetScope with <5 m resolution have potential to improve the mapping of such water bodies in the CEB + S. Generally, the CEB + S does not have high woody vegetation cover, but some areas in Angola do. If some of those areas were inundated, such surface water was largely missed because Landsat sensors are unable to detect surface water under dense vegetation cover. The use of data from Synthetic Aperture Radar (SAR) sensors, for example the European Copernicus Sentinel-1, which have some capability to penetrate the canopy for dense vegetation (DeVries et al., 2020; Hardy et al., 2019; Long et al., 2014; De Groeve, 2010) could further improve the mapping and monitoring of surface water inundation in the CEB + S. Future work should therefore explore the utility of SAR data for operational surface water mapping and flood monitoring in the CEB + S while using maps generated in this study as baseline information.

6. Conclusion

In this study, surface water extent in the CEB + S was estimated and mapped for 32 years (1990–2021) from Landsat data, resulting in the first most accurate baseline information on changes and dynamics of surface water in this human-inhabited endorheic basin. Interannual variability in surface water extent is high in the CEB + S, with water extent increasing almost 15 times during wetter years. A large part of the CEB + S (40%) is however rarely inundated. Rarely inundated areas could become a prime target for human settlements in the future which might contribute to huge socio-economic damages during extreme floods if no precautionary measures are put in place. Therefore, the surface water maps produced in this study provide important baseline information on surface water changes and dynamics in the CEB + S and could therefore support evidence-based spatial planning processes within the basin. The extent and interannual variability of surface water in CEB + S is currently poorly mapped by globally available surface water datasets (JRC and GLAD water extents). With global products unable to provide realistic water extents in CEB + S, there is a need for targeted regular monitoring of surface water extent in the CEB + S to continuously produce surface water maps with local utility to help minimise future impacts of extreme floods.

Declaration of Competing Interest

The authors declare that they have no known competing financial interests or personal relationships that could have appeared to influence the work reported in this paper.

Acknowledgements

This research was implemented thanks to Universities UK International (UUKi) Rutherford Fund Strategic Partner Grants programme that awarded the Fellowships to EH and FP, Aberystwyth University, United Kingdom, in 2018. CT was supported by UK Natural Environment Research Council grant. We are thankful to the anonymous reviewers whose comments greatly improved this manuscript.

References

Allaire, M., 2018. Socio-Economic Impacts of Flooding: A Review of the Empirical Literature. Water Security 3, 18–26. https://doi.org/10.1016/j.wasec.2018.09.002.

Allen, C., Gonzales, R., Parrott, L., 2020. Modelling the contribution of ephemeral wetlands to landscape connectivity. Ecol. Model. 419, 108944. https://doi.org/10.1016/j.ecolmodel.2020.108944.

Alsdorf, E.D., Rodrıguez, E., Lettenmaier, P.D., 2007. Measuring Surface Water from Space. Rev. Geophys. 45, RG2002. https://doi.org/10.1029/2006RG000197.

Álvarez, X., Gómez-Rúa, M., Vidal-Puga, J., 2019. River Flooding Risk Prevention: A Cooperative Game Theory Approach. J. Environ. Manage. 248, 109284. https://doi.org/10.1016/j.jenvman.2019.109284.

Bivand, R., Keitt, T., Rowlingson, B., Pebesma, E., Sumner, M., Hijmans, R., Baston, D., Rouault, E., Frank Warmerdam, F., Ooms, J., Rundel, C., 2018. Bindings for the Geospatial Data Abstraction Library: Package 'Rgdal. R Doc.

Breiman, L., 2001. Random Forests. Mach. Learn. 45, 5–32.

Claverie, M., Ju, J., Masek, G.J., Dungan, L.J., Vermote, F.E., Roger, J., Skakun, V.S., Justice, C., 2018. The Harmonized Landsat and Sentinel-2 Surface Reflectance Data Set. Remote Sens. Environ. 219, 145–161. https://doi.org/10.1016/j.rse.2018.09.002.

Cohen, W.B., Yang, Z., Kennedy, R., 2010. Detecting trends in forest disturbance and recovery using yearly Landsat time series: 2. TimeSync - Tools for calibration and validation. Remote Sens. Environ. 114 (12), 2911–2924.

De Groeve, T., 2010. Flood monitoring and mapping using passive microwave remote sensing in Namibia. Geomat. Natl. Hazards Risk 1 (1), 19–35. https://doi.org/10.1080/19475701003648085.

Deng, Y., Jiang, W., Tang, Z., Ling, Z., Wu, Z., 2019. Long-Term Changes of Open-Surface Water Bodies in the Yangtze River Basin Based on the Google Earth Engine Cloud Platform. Remote Sens. 11 (19), 2213. https://doi.org/10.3390/rs11192213.

DeVries, B., Huang, C., Armston, J., Huang, W., Jones, J.W., Lang, M.W., 2020. Rapid and Robust Monitoring of Flood Events Using Sentinel-1 and Landsat Data on the Google Earth Engine. Remote Sens. Environ. 240, 111664. https://doi.org/10.1016/j.rse.2020.111664.

Di Baldassarre, G., Montanari, A., Lins, H., Koutsoyiannis, D., Brandimarte, L., Blöschl, G., 2010. Flood Fatalities in Africa: From Diagnosis to Mitigation. Geophys. Res. Lett. 37 (22), n/a–n/a. https://doi.org/10.1029/2010GL045467.

Easterling, R.D., Meehl, A.G., Parmesan, C., Changnon, A.S., Karl, R.T., Mearns, O.L., 2000. Climate Extremes: Observations, Modeling, and Impacts. Science 289 (5487), 2068–2074.

Feng, M., Sexton, O.J., Channan, S., Townshend, R.J., 2016. A Global, High-Resolution (30-m) Inland Water Body Dataset for 2000: First Results of a Topographic-Spectral Classification Algorithm. Int. J. Digital Earth 9 (2), 113–133. https://doi.org/10.1080/17538947.2015.1026420.

Feyisa, G.L., Meilby, H., Fensholt, R., Proud, R.S., 2014. Automated Water Extraction Index: A New Technique for Surface Water Mapping Using Landsat Imagery. Remote Sens. Environ. 140, 23–35. https://doi.org/10.1016/j.rse.2013.08.029.

Funk, C.C., Peterson, J.P., Landsfeld, F.M., Pedreros, H.D., Verdin, P.J., Rowland, D.J., Romero, E.B., Husak, J.G., Michaelsen, C.J., Verdin, P.A., 2014. A Quasi-Global Precipitation Time Series for Drought Monitoring. U.S. Geol. Survey Data Ser. 832, 4. https://doi.org/10.3133/ds832.

Gao, B., 1996. NDWI—A Normalized Difference Water Index for Remote Sensing of Vegetation Liquid Water from Space. Remote Sens. Environ. 58 (3), 257–266. https://doi.org/10.1016/S0034-4257(96)00067-3.

Gerland, P., Raftery, A.E., Ševčíková, H., Li, N., Gu, D., Spoorenberg, T., Alkema, L., Fosdick, B.K., Chunn, J., Lalic, N., Bay, G., Buettner, T., Heilig, G.K., Wilmoth, J., 2014. World population stabilization unlikely this Century. Science 346 (6206), 234–237.

Gorelick, N., Hancher, M., Dixon, M., Ilyushchenko, S., Thau, D., Moore, R., 2017. Google Earth Engine: Planetary-Scale Geospatial Analysis for Everyone. Remote Sens. Environ. 202, 18–27. https://doi.org/10.1016/j.rse.2017.06.031.

Government of Namibia, 2009. Post disaster needs assessment: a report prepared by the Government of the Republic of Namibia, with support from the International community. Retrieved from: https://www.met.gov.na/files/files/Namibia%20floods%20Post%20Disaster%20Needs%20Assessment%202009.pdf.

Halabisky, M., Moskal, L.M., Gillespie, A., Hannam, M., 2016. Reconstructing Semi-Arid Wetland Surface Water Dynamics through Spectral Mixture Analysis of a Time Series of Landsat Satellite Images (1984–2011). Remote Sens. Environ. 177, 171–183. https://doi.org/10.1016/j.rse.2016.02.040.

Hardy, A., Ettritch, G., Cross, D.E., Bunting, P., Liywalii, F., Sakala, J., Silumesii, A., Singini, D., Smith, M., Willis, T., Thomas, C.J., 2019. Automatic Detection of Open and Vegetated Water Bodies Using Sentinel 1 to Map African Malaria Vector Mosquito Breeding Habitats. Remote Sens. 11, 593. https://doi.org/10.3390/rs11050593.

Heimhuber, V., Tulbure, G.M., Broich, M., 2016. Modeling 25 Years of Spatio-Temporal Surface Water and Inundation Dynamics on Large River Basin Scale Using Time Series of Earth Observation Data. Hydrol. Earth Syst. Sci. 20 (6), 2227–2250. https://doi.org/10.5194/hess-20-2227-2016.

Hijmans, R.J., van Etten, J., 2015. Raster: Geographic Analysis and Modeling with Raster Data. *R package version 2.5-2*.

Hipondoka, M.H.T., van der Waal, B.C.W., Ndeutapo, M.H., Hango, L., 2018. Sources of Fish in the Ephemeral Western Iishana Region of the Cuvelai-Etosha Basin in Angola and Namibia. Afr. J. Aquat. Sci. 43 (3), 199–214. https://doi.org/10.2989/16085914.2018.1506310.

Hipondoka, M., 2005. The Development and Evolution of Etosha Pan, Namibia. Bayerischen Julius-Maximilians-Universität Würzburg, PhD Thesis.

Huete, A.R., 1988. A Soil-Adjusted Vegetation Index (SAVI). Remote Sens. Environ. 25 (3), 295–309. https://doi.org/10.1016/0034-4257 (88)90106-X.

Isikdogan, F., Bovik, A.C., Passalacqua, P., 2017. Surface Water Mapping by Deep Learning. IEEE J. Sel. Top. Appl. Earth Obs. Remote Sens. 10 (11), 4909–4918.

Kendon, E.J., Stratton, R.A., Tucker, S., Marsham, J.H., Berthou, S., Rowell, D.P., Senior, C.A., 2019. Enhanced future changes in wet and dry extremes over Africa at convection-permitting scale. Nature Commun. 10 (1) https://doi.org/10.1038/s41467-019-09776-9.

Kundzewicz, Z.W., Kanae, S., Seneviratne, S.I., Handmer, J., Nicholls, N., Peduzzi, P., Mechler, R., Bouwer, L.M., Arnell, N., Mach, K., Muir-Wood, R., Brakenridge, G.R., Kron, W., Benito, G., Honda, Y., Takahashi, K., Sherstyukov, B., 2014. Flood Risk and Climate Change: Global and Regional Perspectives. Hydrol. Sci. J. 59 (1), 1–28. https://doi.org/10.1080/02626667.2013.857411.

Lary, D.J., Alavi, H.A., Gandomi, H.A., Walker, L.A., 2016. Machine Learning in Geosciences and Remote Sensing. Geosci. Front. 7 (1), 3–10. https://doi.org/10.1016/j.gsf.2015.07.003.

Li, L., Vrieling, A., Skidmore, A., Wang, T., Turak, E., 2018. Monitoring the Dynamics of Surface Water Fraction from MODIS Time Series in a Mediterranean Environment. Int. J. Appl. Earth Obs. Geoinf. 66, 135–145. https://doi.org/10.1016/j.jag.2017.11.007.

Li, K., Xu, E., 2021. High-accuracy continuous mapping of surface water dynamics using automatic update of training samples and temporal consistency modification based on Google Earth Engine: A case study from Huizhou, China. ISPRS J. Photogramm. Remote Sens. 179, 66–80.

Liaw, A., Wiener, M., 2002. Classification and regression by RandomForest. R News 2 (3), 18–22.

Liu, H.Q., Huete, A., 1995. Feedback Based Modification of the NDVI to Minimize Canopy Background and Atmospheric Noise. IEEE Trans. Geosci. Remote Sens. 33 (2), 457–465. https://doi.org/10.1109/TGRS.1995.8746027.

Long, S., Fatoyinbo, T.E., Policelli, F., 2014. Flood extent mapping for Namibia using change detection and thresholding with SAR. Environ. Res. Lett. 9 (3), 035002. https://doi.org/10.1088/1748-9326/9/3/035002.

Loveland, R.T., Dwyer, L.J., 2012. Landsat: Building a Strong Future. Remote Sens. Environ. 122, 22–29. https://doi.org/10.1016/j.rse.2011.09.022.

Loveland, R.T., Irons, R.J., 2016. Landsat 8: The Plans, the Reality, and the Legacy. Remote Sens. Environ. 185, 1–6. https://doi.org/10.1016/j.rse.2016.07.033.

Masek, J.G., Vermote, E.F., Saleous, N.E., Wolfe, R., Hall, F.G., Huemmrich, K.F., Gao, F., Kutler, J., Lim, T.-K., 2006. A Landsat Surface Reflectance Dataset for North America, 1990–2000. IEEE Geosci. Remote Sens. Lett. 3 (1), 68–72.

Mazzoleni, M., Mård, J., Rusca, M., Odongo, V., Lindersson, S., Di Baldassarre, G., 2021. Floodplains in the Anthropocene: A Global Analysis of the Interplay between Human Population. Water Res. 57 (2) https://doi.org/10.1029/2020WR027744.

Mendelsohn, J., Jarvis, A., Robertson, T., 2013. A Profile and Atlas of the Cuvelai-Etosha Basin. RAISON & Gondwana Collect.

Midzuno, H., 1951. On the Sampling System with Probability Proportionate to Sum of Sizes. Ann. Inst. Stat. Math. 3 (1), 99–107.

Milly, P.C.D., Wetherald, R.T., Dunne, K.A., Delworth, T.L., 2002. Increasing Risk of Great Floods in a Changing Climate. Nature 415 (6871), 514–517. https://doi.org/10.1038/415514a.

Mueller, N., Lewis, A., Roberts, D., Ring, S., Melrose, R., Sixsmith, J., Lymburner, L., McIntyre, A., Tan, P., Curnow, S., Ip, A., 2016. Water Observations from Space: Mapping Surface Water from 25 years of Landsat Imagery across Australia. Remote Sens. Environ. 174, 341–352. https://doi.org/10.1016/j.rse.2015.11.003.

Namibia Statistics Agency, 2011. Namibia 2011 Population and Housing Census Main Report. Retrieved from: https://nsa.org.na/page/publications/.

Niipele, N.J., Chen, J., 2019. The Usefulness of Alos-Palsar Dem Data for Drainage Extraction in Semi-Arid Environments in The Iishana Sub-Basin. J. Hydrol.: Reg. Stud. 21, 57–67. https://doi.org/10.1016/j.ejrh.2018.11.003.

Olofsson, P., Foody, G.M., Stehman, S.V., Woodcock, C.E., 2013. Making Better Use of Accuracy Data in Land Change Studies: Estimating Accuracy and Area and Quantifying Uncertainty Using Stratified Estimation. Remote Sens. Environ. 129, 122–131. https://doi.org/10.1016/j.rse.2012.10.031.

Olofsson, P., Foody, G.M., Herold, M., Stehman, S.V., Woodcock, C.E., Wulder, M.A., 2014. Good Practices for Estimating Area and Assessing Accuracy of Land Change. Remote Sens. Environ. 148, 42–57. https://doi.org/10.1016/j.rse.2014.02.015.

Pekel, J.-F., Cottam, A., Gorelick, N., Belward, A.S., 2016. High-Resolution Mapping of Global Surface Water and Its Long-Term Changes. Nature 540 (7633), 418–422. https://doi.org/10.1038/nature20584.

Pekel, J.F., Vancutsem, C., Bastin, L., Clerici, M., Vanbogaert, E., Bartholomé, E., Defourny, P., 2014. A near real-time water surface detection method based on HSV transformation of MODIS multi-spectral time series data. Remote Sens. Environ. 140, 704–716. https://doi.org/10.1016/j.rse.2013.10.008.

Persendt, F.C., Gomez, C., 2016. Assessment of drainage network extractions in a low-relief area of the Cuvelai Basin (Namibia) from multiple sources: LiDAR, topographic maps, and digital aerial orthophotographs. Geomorphology 260, 32–50. https://doi.org/10.1016/j.geomorph.2015.06.047.

Persendt, F.C., Gomez, C., Zawar-Reza, P., 2015. Identifying Hydro-Meteorological Events from Precipitation Extremes Indices and Other Sources over Northern Namibia, Cuvelai Basin. Jamba 7 (1), 177. https://doi.org/10.4102/jamba.v7i1.177.

Pickens, A.H., Hansen, M.C., Hancher, M., Stehman, S.V., Tyukavina, A., Potapov, P., Marroquin, B., Sherani, Z., 2020. Mapping and Sampling to Characterize Global Inland Water Dynamics from 1999 to 2018 with Full Landsat Time-Series. Remote Sens. Environ. 243, 111792. https://doi.org/10.1016/j.rse.2020.111792.

Pohl, B., Macron, C., Monerie, P.A., 2017. Fewer rainy days and more extreme rainfall by the end of the century in Southern Africa. Sci. Rep. 7, 46466. https://doi.org/10.1038/srep46466.

Qi, J., Chehbouni, A., Huete, A.R., Kerr, Y.H., Sorooshianet, S., 1994. A Modified Soil Adjusted Vegetation Index. Remote Sens. Environ. 48 (2), 119–126. https://doi.org/10.1016/0034-4257(94)90134-1.

R Core Team, 2018. R: A Language and Environment for Statistical Computing. R Foundation for Statistical Computing.

Rahmstorf, S., Coumou, D., 2011. Increase of Extreme Events in a Warming World. Proc. Natl. Acad. Sci. 108 (44), 17905–17909. https://doi.org/10.1073/pnas.1101766108.

Rouse, J.W., Haas, R.H., Schell, J.A. & Deeering, D.W., 1973. Monitoring Vegetation Systems in the Great Plains with ERTS (Earth Resources Technology Satellite). In: Proceedings of the Third 80 ERTS Symposium; NASA SP-351; NASA: Washington, DC, USA, pp. 309–317.

Schmidt, G., Jenkerson, C., Masek, J. G., Vermote, E. F., Gao, F., 2013. Landsat Ecosystem Disturbance Adaptive Processing System (LEDAPS) Algorithm Description. In: U.S. Geological Survey Open-File Report 2013. U.S. Geological Survey, pp. 17. https://pubs.usgs.gov/of/2013/1057/ofr13_1057.pdf (accessed date: 10 January 2021).

Seiler, R., Schmidt, J., Diallo, O., Csaplovics, E., 2009. Flood Monitoring in a Semi-Arid Environment Using Spatially High Resolution Radar and Optical Data. J. Environ. Manage. 90 (7), 2121–2129. https://doi.org/10.1016/j.jenvman.2007.07.035.

Shao, Z., Cai, J., Fu, P., Hu, L., Liu, T., 2019. Deep Learning-Based Fusion of Landsat-8 and Sentinel-2 Images for a Harmonized Surface Reflectance Product. Remote Sens. Environ. 235, 111425. https://doi.org/10.1016/j.rse.2019.111425.

Stehman, S.V., 2009. Sampling Designs for Accuracy Assessment of Land Cover. Int. J. Remote Sens. 30 (20), 5243–5272. https://doi.org/10.1080/01431160903131000.

Stehman, S.V., 2012. Impact of Sample Size Allocation When Using Stratified Random Sampling to Estimate Accuracy and Area of Land-Cover Change. Remote Sens. Lett. 3 (2), 111–120. https://doi.org/10.1080/01431161.2010.541950.

Svetlana, D., Radovan, D., Ján, D., 2015. The Economic Impact of Floods and Their Importance in Different Regions of the World with Emphasis on Europe. Procedia Econ. Finance 34, 649–655. https://doi.org/10.1016/S2212-5671(15)01681-0.

Sweet, J., 1998. Livestock: Coping with drought. Namibia: A case study, London: Overseas Development Institute. Network paper.

Takaku, J., Tadono, T., Tsutsui, K., Ichikawa, M., 2018. Quality Improvements of 'AW3D' Global DSM Derived from Alos Prism. In: IGARSS 2018 – 2018 IEEE International Geoscience and Remote Sensing Symposium, Valencia, Spain, pp. 1612–1615. https://doi.org/10.1109/IGARSS.2018.8518360.

Taukeni, S., Chitiyo, G., Chitiyo, M., Asino, I., Shipena, G., 2016. Post-traumatic stress disorder amongst children aged 8–18 affected by the 2011 northern-Namibia floods. Jamba 8 (2), 169. https://doi.org/10.4102/jamba.v8i2.169.

Tellman, B., Sullivan, J.A., Kuhn, C., Kettner, A.J., Doyle, C.S., Brakenridge, G.R., Erickson, T.A., Slayback, D.A., 2021. Satellite imaging reveals increased proportion of population exposed to floods. Nature 596 (7870), 80–86. https://doi.org/10.1038/s41586-021-03695-w.

Tucker, C.J., 1979. Red and Photographic Infrared Linear Combinations for Monitoring Vegetation. Remote Sens. Environ. 8 (2), 127–150. https://doi.org/10.1016/0034-4257 (79)90013-0.

Tulbure, M.G., Broich, M., 2013. Spatiotemporal Dynamic of Surface Water Bodies Using Landsat Time-Series Data from 1999 to 2011. ISPRS J. Photogramm. Remote Sens. 79, 44–52. https://doi.org/10.1016/j.isprsjprs.2013.01.010.

Tulbure, M.G., Kininmonth, S., Broich, M., 2014. Spatiotemporal Dynamics of Surface Water Networks across a Global Biodiversity Hotspot - Implications for Conservation. Environ. Res. Lett. 9 (11), 114012. https://doi.org/10.1088/1748-9326/9/11/114012.

Tulbure, M.G., Broich, M., Stehman, S.V., Kommareddy, A., 2016. Surface Water Extent Dynamics from Three Decades of Seasonally Continuous Landsat Time Series at Subcontinental Scale in a Semi-Arid Region. Remote Sens. Environ. 178, 142–157. https://doi.org/10.1016/j.rse.2016.02.034.

Tulbure, M.G., Broich, M., Perin, V., Gaines, M., Ju, J., Stehman, S.V., Pavelsky, T., Masek, J.G., Yin, S., Mai, J., Betbeder-Matibet, L., 2022a. Can we detect more ephemeral floods with higher density harmonized Landsat Sentinel 2 data compared to Landsat 8 alone? ISPRS J. Photogramm. Remote Sens. 185, 232–246. https://doi.org/10.1016/j.isprsjprs.2022.01.021.

Tulbure, M.G., Hostert, P., Kuemmerle, T., Broich, M., Disney, M., Hernández-Stefanoni, J., 2022b. Regional matters: On the usefulness of regional land-cover datasets in times of global change. Remote Sens. Ecol. Conserv. 8 (3), 272–283. https://doi.org/10.1002/rse2.248.

United Nations, 2017. World Population Prospects World Population Prospects: The 2017 Revision. Retrieved from https://population.un.org/wpp.

Vermote, E., Justice, C., Claverie, M., Franch, B., 2016. Preliminary Analysis of the Performance of the Landsat 8/OLI Land Surface Reflectance Product. Remote Sens. Environ. 185, 46–56. https://doi.org/10.1016/j.rse.2016.04.008.

Wang, C., Jia, M., Chen, N., Wang, W., 2018. Long-Term Surface Water Dynamics Analysis Based on Landsat Imagery and the Google Earth Engine Platform: A Case Study in the Middle Yangtze River Basin. Remote Sensing 10 (10), 1635. https://doi.org/10.3390/rs10101635.

Wulder, M.A., Masek, J.G., Cohen, W.B., Loveland, T.R., Woodcock, C.E., 2012. Opening the Archive: How Free Data Has Enabled the Science and Monitoring Promise of Landsat. Remote Sens. Environ. 122, 2–10. https://doi.org/10.1016/j.rse.2012.01.010.

Wulder, M.A., Hilker, T., White, J.C., Coops, N.C., Masek, J.G., Pflugmacher, D., Crevier, Y., 2015. Virtual Constellations for Global Terrestrial Monitoring. Remote Sens. Environ. 170, 62–76. https://doi.org/10.1016/j.rse.2015.09.001.

Xia, H., Zhao, J., Qin, Y., Yang, J., Cui, Y., Song, H., Ma, L., Jin, N., Meng, Q., 2019. Changes in Water Surface Area during 1989–2017 in the Huai River Basin Using Landsat Data and Google Earth Engine. Remote Sensing. 11, 1824. https://doi.org/10.3390/rs11151824.

Xu, H., 2006. Modification of Normalised Difference Water Index (NDWI) to Enhance Open Water Features in Remotely Sensed Imagery. Int. J. Remote Sens. 27 (14), 3025–3033. https://doi.org/10.1080/01431160600589179.

Yang, X., Qin, Q., Yésou, H., Ledauphin, T., Koehl, M., Grussenmeyer, P., Zhu, Z., 2020. Monthly Estimation of the Surface Water Extent in France at a 10-m Resolution Using Sentinel-2 Data. Remote Sens. Environ. 244, 111803. https://doi.org/10.1016/j.rse.2020.111803.

Zhu, Z., Woodcock, C.E., 2012. Object-Based Cloud and Cloud Shadow Detection in Landsat Imagery. Remote Sens. Environ. 118, 83–94. https://doi.org/10.1016/j.rse.2011.10.028.

Zhu, Z., Wang, S., Woodcock, C.E., 2015. Improvement and Expansion of the Fmask Algorithm: Cloud, Cloud Shadow, and Snow Detection for Landsats 4–7, 8, and Sentinel 2 Images. Remote Sens. Environ. 159, 269–277. https://doi.org/10.1016/j.rse.2014.12.014.

Zhu, Z., Woodcock, C.E., 2014. Automated Cloud, Cloud Shadow, and Snow Detection in Multitemporal Landsat Data: An Algorithm Designed Specifically for Monitoring Land Cover Change. Remote Sens. Environ. 152, 217–234. https://doi.org/10.1016/j.rse.2014.06.012.